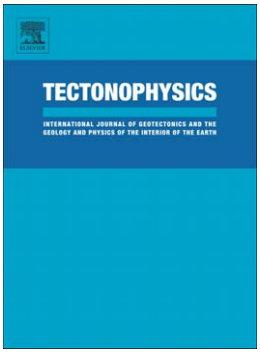

Kinematics, seismotectonics and seismic potential of the eastern sector of the European Alps from GPS and seismic deformation data

E. Serpelloni, G. Vannucci, L. Anderlini, R.A. Bennett

PII: S0040-1951(16)30391-2
DOI: doi: 10.1016/j.tecto.2016.09.026
Reference: TECTO 127258

To appear in: *Tectonophysics*

Received date: 29 June 2016
Revised date: 15 September 2016
Accepted date: 23 September 2016

Please cite this article as: Serpelloni, E., Vannucci, G., Anderlini, L., Bennett, R.A., Kinematics, seismotectonics and seismic potential of the eastern sector of the European Alps from GPS and seismic deformation data, *Tectonophysics* (2016), doi: 10.1016/j.tecto.2016.09.026

Kinematics, Seismotectonics and Seismic Potential of the Eastern Sector of the European Alps from GPS and Seismic Deformation Data

Serpelloni E. [1*], G. Vannucci [2], L. Anderlini [1], R.A. Bennett [3]

[1)] Istituto Nazionale di Geofisica e Vulcanologia, Centro Nazionale Terremoti

[2)] Istituto Nazionale di Geofisica e Vulcanologia, Sezione di Bologna

[3)] Dept. of Geoscience, University of Arizona, Tucson (AZ), USA

*Corresponding author

Enrico Serpelloni

Istituto Nazionale di Geofisica e Vulcanologia

Via D. Creti 12, 40128 – Bologna (IT)

Emai: enrico.serpelloni@ingv.it

Phone: +39 051 4151433

Abstract

We present a first synoptic view of the seismotectonics and kinematics of the eastern sector of the European Alps using geodetic and seismological data. The study area marks the boundary between the Adriatic and the Eurasian plates, through a wide zone of deformation including a variety of tectonic styles within a complex network of crustal and lithospheric faults. A new dense GPS velocity field, new focal mechanisms and seismic catalogues, with uniformly re-calibrated magnitudes (from 1005), are used to estimate geodetic and seismic deformation rates and to develop interseismic kinematic and fault locking models. Kinematic indicators from seismological and geodetic data are remarkably consistent at different spatial scales. In addition to large-scale surface motion, GPS velocities highlight more localized deformation features revealing a complex configuration of interacting tectonic blocks, for which new constraints are provided in this work accounting for elastic strain build up at faults bonding rotating blocks. The geodetic and seismological data highlight two belts of higher deformation rates running WSW-ENE along the Eastern Southern Alps (ESA) in Italy and E-W in Slovenia, where deformation is more distributed. The highest geodetic strain-rates are observed in the Montello-Cansiglio segment of the ESA thrust front, for which the higher density of the GPS network provides indications of limited interseismic locking. Most of the dextral shear between the Eastern Southern Alps and the Eastern Alps blocks is accommodated along the Fella-Sava fault rather than the Periadriatic fault. In northern Croatia and Slovenia geodetic and seismological data allow constraining the kinematics of the active structures bounding the triangular-shaped region encompassing the Sava folds, which plays a major role in accommodating the transition from Adria- to Pannonian-like motion trends. The analysis of the seismic and geodetic moment rates provides new insights into the seismic potential along the ESA front.

Keywords: European Alps; Seismotectonics; Microplate Kinematics; Global Positioning System; Seismic Potential

1. INTRODUCTION

Continental earthquakes are one of the most widely observable indicators of active intraplate deformation. Although sparser in time than large earthquakes occurring at the edges of oceanic and continental plates, the economic and social impacts of earthquakes within diffuse zones of continental deformation is huge, because of the presence of important and ancient human and industrial settlements, key transportation infrastructures, and a unique

historical and monumental heritage, with consequent high exposure to significant damages (e.g., Bilham, 2013). Diffuse deformation, slow tectonic rates, and long repeat times of large earthquakes make the estimates of seismic hazard at continental plate boundaries a challenging task. This is the case of the Alps, which are a classic example of a broadly deforming continental collisional belt (Schmid et al., 2004). Present-day convergence between the Adriatic microplate and the Eurasian plate is mainly accommodated in the eastern European Alps (D'Agostino et al., 2005; Bechtold et al., 2009; Cheloni et al., 2014), where the Adriatic lithosphere underthrusts the Alpine mountain belt. The northernmost tip of this convergent margin is located at the border between Italy, Austria and Slovenia. Here, the S-verging fold-and-thrust belt of the Eastern Southern Alps (ESA), the W- SW- verging Dinaric belt and the ~E-W structures belonging to the Carpathians system interact, creating a puzzlingly diffuse tectonic boundary.

The ESA is the locus of strong (M>6) earthquakes occurred in the past (Fig. 1). Information from historical sources and modern earthquake catalogs show that there were at least 12 earthquakes with a magnitude of ≥6 in the past thousand years. The last one took place in 1976 in northern Italy (Mw 6.46, Rovida et al., 2011), followed by two aftershocks with magnitudes greater than 6 within a few months (Pondrelli et al., 2001). This earthquake sequence claimed 989 lives and injured 2,400 people; about 45,000 were left homeless as a result. Although the extent of damage for historical events can sometimes be difficult to estimate, it is likely that at least three of the quakes shown in Fig. 1 caused more than 10,000 deaths. While for some of these earthquakes authors generally agree that the fault sources belong to the ESA thrust fault system, emerging at the boundary between the Venetian plane and the mountain front in northeastern Italy (Benedetti et al., 2000; Burrato et al., 2008; Galadini et al., 2005; Cheloni et al., 2013), for others, the fault sources are still uncertain. This is the case of the 1117 (Mw ~6.7) Verona earthquake, the 1348 (Mw ~7) Carinzia earthquake and the 1511 Slovenia (Mw ~6.9) earthquake (Rovida et al., 2011, Stucchi et al., 2012).

Uncertainties on the location, geometry and seismic potential of active faults in the Eastern Alps persists due: i) to the complex structural framework of the region, inherited by the geodynamic evolution of this area and resulting in deformation distributed over a vast area, ii) slow deformation rates at mainly blind faults, iii) sparse instrumental seismicity, causing some areas where strong historical earthquakes occurred to appear presently almost aseismic (see Fig. 1). In this framework Global Positioning System (GPS) data provide fundamental constraints on the kinematics of continental deformation. GPS observations, in fact, have provided increasingly more details on the kinematics of this area (e.g., Grenerczy et

al., 2005, Caporali et al., 2013), fault slip-rates (e.g., D'Agostino et al., 2005; Bechtold et al., 2009; Barba et al., 2013) seismic potential (e.g., Bus et al., 2009; Cheloni et al., 2014) and geodynamics (e.g., Metois et al., 2015).

The kinematic boundary conditions in the ESA of Italy are well known, with ~N-S convergence rates increasing from west to east as resulting from the counterclockwise rotation of the Adriatic microplate around a pole of rotation located in the western Po Plain (Nocquet and Calais, 2003; Battaglia et al., 2004; Serpelloni et al., 2005; D'Agostino et al., 2008). Deformation indicators from geodesy and seismotectonics are in fairly good agreement in the Italian ESA, making assumptions on the kinematics and location of active faults there more robust. On the contrary, at the boundary between Italy, Austria and Slovenia, where different tectonic regimes coexist (e.g., Bressan et al., 2003; Poli and Renner, 2004; Herak et al., 2009) and GPS stations are sparser, uncertainties on the location and kinematics of major active faults are larger.

This work focuses on the Eastern Southern Alps (ESA), south of Lat. 48°N, where the number of geodetic and seismic data is greater and both tectonic rates and seismic hazard are higher than the Eastern Alps. We use a new earthquake catalogue, with original and proxies (i.e., recalibrated) moment magnitudes (Mw), from 1005 to present-days, and a new dataset of focal mechanisms (FM) that provide a detailed seismotectonic map of the area. A new GPS velocity field, obtained from the analysis of continuous and survey-mode GPS stations (260 sites between longitude 9-17°E and latitude 44-48°N), is used to study crustal deformation, microplate and tectonic block kinematics and fault slip rates. Despite the debate about the proper model for representing diffuse continental deformation (e.g., Thatcher, 2003; Aktug et al., 2009; Floyd et al., 2010), for the purposes of this study we use an elastic block model approach (McCaffrey, 2002; Meade and Loveless, 2009). The main advantage of block models, with respect to a continuous deformation description, is that they allow estimation of fault slip rates that are required to constrain the degree of interseismic locking on the fault surface, and consequently provide inferences on the seismogenic potential of active faults. The drawback is that some hypotheses on the blocks boundaries must be prescribed. By comparing the seismic moment release rates with geodetically determined moment rates, quantified in terms of seismic and geodetic flux (i.e., moment rates per unit area) we provide new insights into the seismic potential of the study area.

2. GEOLOGIC AND STRUCTURAL OUTLINES

The Alps were developed from the Cretaceous onwards by subduction of a Mesozoic ocean followed by collision between the Adriatic (Austroalpine-Southalpine) and European (Penninic-Helvetic) continental margins. The continent- continent collision started after the subduction and thrusting of the Penninic flysch units, during the Eocene (~50 Ma) (Decker and Peresson, 1996). According to the direction of tectonic transport, the Alps are subdivided into two belts of differing size, age and geological significance (see Fig.1): 1) the Europe-verging belt, a thick collisional wedge of Cretaceous-Neogene age (~145-2.5 Ma), consisting of continental and minor oceanic units radially displaced towards the Molasse foredeep and European foreland; 2) the Southern Alps, a minor, shallower (non-metamorphic) and younger (Neogene, ~23 Ma) thrust-and-fold belt displaced to the south (Adria-verging), which developed within the Alpine hinterland of the Adriatic upper plate. The two belts are separated by the Periadriatic lineament, or Periadriatic fault (PAF, see Fig.1), a major fault system of Oligocene-Neogene age (~34-2.5 Ma).

This work focuses on the eastern sector of the Alpine belt, which is part of the Alpine, Carpathian, Dinaridic system (AlCaDi after Schmidt et al., 2008). The Eastern Alps (see Fig.1 for toponyms) are bounded to the west by the Brenner normal fault, to the north by the European foreland, with the Bohemian Massif and Molasse basin, and to the east and far east by the Pannonian basin and the Western Carpathians, respectively. The southern boundary is marked by the PAF, south of which are the Dinarides and the Southern Alps (see inset in Fig. 1).

The study area is a typical example of an orogenic system formed by indenting one continent into another (continent-continent collision). Within this model, the rigid Adriatic microplate has indented obliquely into a softer region along the southern margin of the European plate (Ratschbacher et al., 1991a, 1991b; Frisch et al., 1998). This indenter model is consistent with the overall geometry of the Alps, with the region of maximum horizontal shortening being located north of the indenter front and with long, orogen-parallel structures that fan out toward the east and extrude the orogen eastward toward the Pannonian Basin (Fig.1). North of the PAF, part of the shortening is accommodated by lateral extrusion and tectonic escape of the Austroalpine units toward the east (Ratschbacher et al., 1991b) along a corridor formed by the dextral PAF to the south and the sinistral Innsbruck–Salzburg–Amstetten (ISAM), Salzach–Enns–Mariazell–Puchberg (SEMP) and Mur Mürz faults to the north (Fig. 1). Eastward extrusion started in Oligocene times (~34 Ma) mainly on the ISAM and PAF faults (Wölfler et al., 2011). Activity moved to the SEMP fault, which has served as the northern border of the extruding block since early Miocene.

The Southern Alps are a typical example of a deformed passive continental margin in a mountain range (Bertotti et al., 1993). Until the Oligocene, this Adriatic domain was the gently deformed retro-wedge hinterland of the Alps, intensively reworked only at its eastern edge by the Paleogenic Dinaric belt. From the Neogene (~23 Ma), the Southalpine fold-and-thrust belt developed and progressively propagated toward the Adriatic foreland, mainly reactivating Mesozoic (~250-65 Ma) extensional faults (Castellarin et al., 1992). The ESA southern front is now mainly buried beneath the alluvial deposits of the Venetian plain and sealed by Late Miocene to Quaternary (~7-2.5 Ma) deposits.

The Venetian sector of the (ESA) fold-and-thrust belt is dominated by the SE-verging Bassano-Valdobbiadene thrust (Doglioni 1992; Burrato et al., 2005), a major structure that has produced a morphological relief of ~1200 m above the plain (Fig. 1). In the westernmost sector, the thrust is crossed by the NW–SE trending Schio-Vicenza (SV in Fig. 1) strike-slip fault system, a Late Miocene-Quaternary kinematic junction between the ESA and the Central-Western Southern Alps (Castellarin & Cantelli 2000). The Schio-Vicenza line borders to the east the Giudicarie-Lessini region, a triangular-shaped block wedged with its apex into the Neogene Southern Alps fold-and-thrust belt. This block represents a tectonic boundary between the central-western and the ESA (e.g., Laubscher, 1996; Massironi et al. 2006). East of the Schio-Vicenza line, the southernmost front of the ESA in Veneto consists of (Fig. 1) the Thiene-Bassano and Bassano-Cornuda thrusts and the Montello thrust (e.g. Benedetti et al. 2000; Fantoni et al. 2001; Galadini et al. 2005; Burrato et al., 2008; Danesi et al., 2015). In the Friuli ESA the most recent compressive front affects the base of the Venetian and Carnic Alps and corresponds to the WSW–ENE striking Polcenigo-Maniago and Arba-Ragogna thrusts (Poli et al. 2002; Galadini et al., 2005). In the eastern (i.e., Julian) sector of the ESA the front extends southward to the lower Friulian plain (Poli et al. 2002). In the Udine-Gorizia sector it corresponds to a set of S-verging, WNW–ESE trending low-angle thrusts geometrically influenced by the inherited structures of the NW–SE Dinaric Palaeogene front (Fig. 1).

The eastward extent of the ESA thrust belt is controversial. Southern and southwestern Slovenia is extensively faulted by NW-SE-trending dextral faults, which form conspicuous topographic lineaments, particularly in karstic areas, such as the Idrja and Raša faults (Fig. 1). Since the faults are parallel to the strike of Dinaric folds and thrusts, they are classically called Dinaric faults although no structural connection with Dinaric thrusting is known. These faults cut and displace both Dinaric and South-Alpine fold-and-thrust structures. In the Julian Alps and western Slovenia, the South-Alpine front overthrusted and refolded Dinaric thrust structures (Doglioni, 1987; Placer and Car, 1998). The south Alpine thrusts of the Julian Alps in

western Slovenia continue into the Valsugana thrust system in Italy of mid- to late Miocene age (e.g., Castellarin and Cantelli, 2000). Thrust sheets exposed in the Sava Folds region (Fig. 1) are considered as south-Alpine, due to the paleogeographic affinities of the thrust units (e.g., Placer, 1999), but Oligocene sediments apparently cover the thrusts (Placer, 1999b), implying that thrusting in the Sava Folds region pre-dates the Miocene South-Alpine episode. Also the Post-Oligocene thrusts of the Kamnik Alps are South-Alpine, however the entire unit was probably subsequently displaced eastward several tens of kilometers along the dextral Sava fault (see Fig.1). Therefore, the eastern boundary of ESA thrust front originally could have been at the present-day longitude of the Julian Alps in western Slovenia.

The PAF zone represents a major topographic and structural boundary in northern Slovenia. The E-W- to NW-SE-trending, gently curved dextral Sava fault south of the PAF has impressive topographic expression. Towards the west in Italy, where the Sava fault is known as the Fella Line, the slip sense gradually changes to reverse dextral, and the fault merges with the South-Alpine thrusts. Eastward, the Sava fault merges with the Šoštanj fault and the Labot fault, together forming the continuation of the PAF zone towards the Drava graben.

3. SEISMOTECTONICS

In this work several historical and instrumental earthquake catalogues and FMs catalogues are integrated with the goal of characterizing and analyzing the pattern of seismic moment release and the tectonic regimes of the study area.

3.1 Seismicity and focal mechanisms

Fig. 1 displays the seismicity obtained by merging earthquakes available from 1005 to the end of 2014. In particular, in this work we merge: *i*) the Catalogo Parametrico dei Terremoti Italiani (CPTI, Rovida et al., 2011), *ii*) the SHARE European Earthquake Catalogue (SHEEC, Stucchi et al., 2012), *iii*) the International Seismological Centre Bullettin (ISC, 2014) and *iv*) the catalogue of homogeneous magnitude Mw in Italy (MRGGA, Gasperini et al., 2012, 2013a,b, Lolli et al., 2014, 2015). All these catalogues cover different time spans (see Table S1), with some overlaps, and are originally provided with different type of magnitudes (Ml, Ms, mb, etc.) not homogeneously determined. In order to overcome this problem, several recently defined regressions (Gasperini et al., 2012, 2013a, b; Lolli et al., 2014, 2015) are used in order to re-evaluate consistently all of the magnitudes in Mw. The MRGGA catalogue, which originally starts from 1981, is first extended back to 1960 the by adding the open file CAING of the Istituto Nazionale di Geofisica. The seismicity is then extended backward in time up to 1005 adding

earthquakes from the ISC Bulletin (ISC, 2014) and from CPTI and SHEEC catalogues, where all the Mw are re-evaluated following Gasperini et al. (2013b) and Lolli et al. (2014).

When catalogues overlap in space and time two criteria have been adopted to select a single event. If the earthquake is located inside the "CPTI area", roughly corresponding to the Italian area, the event from a preferred catalogue is chosen among those available by using a weighting scheme that assign a preference order: 1) MRGGA, 2) CPTI, 3) ISC, 4) SHEEC. If the earthquake is outside the CPTI-Italian area the following weighting scheme is adopted: 1) ISC, 2) SHEEC, 3) MRGGA, 4) CPTI. The merged catalogue (MRGC) includes ~77,000 earthquakes in the study area (Fig. 1). The spatial distribution covered by the different seismic catalogues is shown in Fig. S1.

Earthquake FMs for the study area are available from several global and regional catalogues, and are usually derived from different seismogram modeling approaches. More specifically, FMs for the study area are available from i) the Global Centroid Moment Tensor project (GCMT, Dziewonski et al., 1981; Ekström et al, 2005), ii) the National Earthquake Information Center (NEIC, Sipkin, 1982, 1994) of the U.S. Geological Survey, iii) the *Eidgenössische Technische Hochschule Zürich* (ETHZ, Braunmiller et al, 2002), iv) the European-Mediterranean Regional Centroid Moment Tensor (RCMT, Pondrelli et al. (2011) and references therein and quick RCMT on-line available at: http://autorcmt.bo.ingv.it/quicks.html), v) the Time Domain Moment Tensor (TDMT, Scognamiglio et al., 2009 and automatic TDMT on-line available at: http://cnt.rm.ingv.it/tdmt.html), vi) the Earthquake Mechanisms of the Mediterranean Area (EMMA, Vannucci et al., 2003, 2004, 2010) database, which collects focal solutions (mainly first-pulse) available in the literature. The EMMA database has been updated for this work considering additional FMs for the study area. When more than one focal solution is available for the same event in different catalogues, the criterion described in Vannucci and Gasperini (2004) is adopted for selecting a preferred FM solution. For the study area the merged dataset of preferred FMs includes ~1,050 data. Fig. S2a in the supplementary material shows the FMs available with different colors corresponding to the original data sources.

3.2 Seismic flux

By using an approach similar to that described in Serpelloni et al. (2007) the MRGC is used to estimate the seismic (i.e., co-seismic) flux, that is the energy released (the seismic moment released) per unit time (year) and per unit area (km^2) by the earthquakes in the combined catalog. In contrast to a map of hypocenters, a map of the seismic flux provides a more synthetic view of the seismically active lineaments and faults in space and in time. The

seismic flux cannot be considered as representative of the whole amplitude of active strains, but represents a quantitative and qualitative tool to outline its spatial distribution. In particular, the qualitative aspect (i.e., spatial definition of the seismic deformation areas) increases when the time interval decreases, due to the short time coverage of the seismic catalogue.

The scalar seismic moment released (in dyne*cm) per unit area (in km^2) and per year is computed for each 0.1°x0.1° cell of a regular grid, considering different time intervals, and in particular the 1005-2014, 1600-2014, 1905-2014 and 1960-2014 time intervals. The choice of these different time intervals is not arbitrary, representing, at least for the Italian region, the periods covered by the four available seismic catalogues. While the 1005-2014 time-span includes the whole seismic information available, extended to pre-instrumental epochs using historical data from the CPTI and SHEEC catalogues, the 1600-2014 interval represents the range in which the CPTI (historical) catalogue is complete for magnitudes greater than 5.5. The 1905-2014 interval represents the range of the ISC catalogue, i.e., of the first instrumental magnitudes available for the study area. The 1960-2014 is the time-span of availability of the instrumental catalogue from the Italian seismic network. For each earthquake the radius of the seismic crack (i.e. the semi-length of the seismogenic fault derived from the scalar seismic moment of each event) has been estimated from standard scaling relationships (Kanamori & Anderson, 1975) in order to determine the percentage of the seismic crack area (and then of the scalar seismic moment) falling into each cell of the grid to be considered in the seismic moment summation (see Serpelloni et al., 2007 for more details). We do not use a fixed seismogenic depth to select crustal earthquakes, but the EPcrust (Molinari and Morelli, 2011) model that provides depth surfaces for the upper crust, lower crust and Moho. The upper crust (UPC) layer represents a conservative representation of the seismogenic/brittle layer for selecting the earthquakes to be used in the computation of the seismic flux. For events in the CPTI and SHEEC catalogues for which hypocentral depths are not provided we assign a-priori UPC depths.

The seismicity confined between the Earth's surface and UPC depth (Fig. S4a) represents >95% of the earthquakes in the MRGC (Fig. S4b). Following Chiarabba et al. (2005), we also define the depth of the seismogenic layer from the analysis of the seismicity cut-off. The 75% of seismicity cut-off is computed in each cell for which at least 10 events are present, using only earthquakes located within the upper crust (Fig. S4c). The depth of the seismogenic layer from the 75% percentile is ~30-40% lower than the UPC depth, moving this surface up of ~6-10 km (see Fig. S4). Using this surface as the seismogenic layer for selecting earthquakes in the

calculation of the seismic flux causes the elimination of ~12,000 earthquakes (i.e., ~16% of the data-set of earthquakes in the UPC) without, however, significantly changing the estimated seismic flux. Figure S5 in the supplementary material shows a continuous map of the seismogenic layer estimated using the method of Tape et al. (2009).

Figure 2 shows smoothed maps of the seismic flux, starting from the "raw data" in the 0.1°x0.1° cells (Fig. S3), obtained by adopting an adjustable tension continuous curvature surface gridding algorithm (Smith and Wessel, 1990), for the four time intervals considered. By using the maximum temporal interval available in the MRGC (since 1005, Fig. 2A) the seismic flux highlights the areas with stronger seismic activity corresponding to the main active tectonic lineaments in the study area. In particular, the ESA fold-and-thrust belt displays an about continuous SW-NE oriented lineament of seismic flux extending from the Montello thrust toward the east, where the Friuli-Austria border and Carnic Alps shows the highest seismic flux of the study region (mostly associated to the 1690, 1794 and 1976 Mw>6 earthquakes). Further to the east, the map of the seismic flux highlights a NW-SE (i.e., Dinaric) oriented lineament in Slovenia and Croatia, and a broad zone of higher seismic flux corresponding to the triangular-shaped region confined to the north by the Sava fault and to the south by the Sava folds. West of the Montello segment, high seismic flux values correspond to the area of the 1117 Verona earthquake, while the ESA segment between the Lessini mountains and the Montello hill is almost aseismic. To the west, higher seismic flux values are present west of the Lake of Garda along the Sarca fault system.

Considering the shorter time-span (Fig. 2D), i.e. the last 50 years, only the Friuli sector, the Dinaric system in Slovenia and northern Croatia and the triangular-shaped area encompassing the Sava fault and Sava folds displays relatively higher seismic flux values, with the southernmost fold-and-thrust belt in the Venetian alps, including the area south of Verona, being characterized by low values of the seismic flux.

As regard the Eastern Alps, north of the PAF, Fig. 2 highlights some lineaments characterized by higher seismic flux values, which represent spatially persistent features over different time-intervals, including the Brenner fault and the westernmost portion of the Inntal line, and to the east the Mur-Mürz fault. The highest seismic flux values north of the PAF are located in correspondence of the 1348 and 1690 earthquakes at the border between Italy and Austria, but the same area appears almost aseismic, with respect to its surroundings, from 1900.

3.3 Tectonic regimes

We analyze the catalogue of FMs (see Fig. 2 and Fig. S2) deriving the seismic strain tensors over the study area, following well-known seismic moment tensor summation procedures (e.g. Kostrov 1974; Jackson & McKenzie 1988; Westaway 1992; Pondrelli *et al.* 1995; Vannucci *et al.* 2004, Serpelloni et al., 2007). We do not attempt to compute seismic strain rates, limiting the analysis to principal strain orientations that are reasonably representative of the prevailing tectonic regimes in the study area. It is worth noting that where rapid transitions between different regimes are likely to occur, or where a great variability of the tectonic regimes is present, this choice can lead to the sum of non-coherent focal solutions.

The seismic strain tensors are derived in hexagonal equiareal cells with 10 km of side. As for the computation of the seismic flux, the upper crust from the EPcrust model (Molinari and Morelli, 2011) has been used as depth of the seismogenic/brittle layer, within which FMs to be summed are selected. In particular, the mean of depth nodes of the EPcrust model is computed within each hexagonal cell to select FMs in UPC thickness and then compute the weighted (by original or proxy Mw magnitude) contribution of each focal solution to the FM sum of each cell. Fig. 3b shows the tectonic regimes using the Frohlich (1992) ternary diagram representation. Each FM sum is identified with a point within the ternary diagram and with a RGB color corresponding to the tectonic regime, where the red color corresponds to a purely compressive regime, the green color to strike-slip regime and the blue color to purely extensional regime, while a composite color indicates mixed tectonic regime (see legend in the inset of Fig. 3b. Figure 3b shows also the principal seismic strain directions as horizontal projections of maximum compression (P) and traction (T) axes of the cumulative moment tensor in each hexagonal cell. Individual FMs (Fig. 3a) and their representation in terms of areal deformation with main strain directions (Fig. 3b) underline some key features of the styles of tectonic deformation in the study area. Fig. S2b shows the results plotted in terms of beach balls.

The western sector of the study area (i.e., close to the Garda Lake and Lessini mountains) is characterized by prevailing strike-slip and compressional events, with about N-S oriented P-axes accordingly to the direction of convergence predicted by the Adria-Eurasia rotation pole (dashed gray lines in Fig. 3b) calculated from the GPS velocities (see Section 4). The Montello-Cansiglio segment of the ESA fold-and-thrust belt, between Lon. 11.5°E and 12.5°E, is characterized by prevailing strike-slip regimes and smaller thrust-faulting events, with P-axes that appear overall rotated, in a counterclockwise sense, with respect to the Adria-Eurasia direction of convergence. It is worth noting that FMs in the Montello area come from local, short-term, seismic experiments (Danesi et al., 2015).

In the Friuli ESA, between Lon. 12.5°E and 13.5°E, the tectonic regimes are mainly compressional, with P-axes well aligned along the NNW-SSE Adria-Eurasia convergence directions. Although not well mapped by the summation procedure because of the vicinity of earthquakes with different regimes and prevalence of inverse events, two of the northernmost FMs of the Friuli cluster, close to the Fella line, show right-lateral strike slip regimes. To the north, along the PAF FMs are present only in its Slovenian segment, with compressional regimes and NNE-SSW oriented P-axes. Along the southern branch of the PAF, the Sava-Celje faults, mainly right-lateral motion and N-S thrust faulting along ~E-W faults are present.

In the ESA of Slovenia and northern Croatia, the prevailing tectonic regime is strike-slip to thrust faulting. Along the NW-SE oriented Dinaric lineaments, roughly corresponding to the Raša fault, the P-axes are NNE-SSW oriented and counterclockwise rotated with respect to the ~N-S Adria-Eurasia convergence direction. To the south, along the coasts of northern Croatia, the tectonic regime is mainly compressional, with P-axes aligned to the Adria-Eurasia convergence direction. The Slovenian Alps are characterized by a prevailing strike-slip regime. In particular, both the Sava folds and Sava fault zones display strike-slip tectonics with prevailing N-S oriented P-axes.

In the Eastern Alps, strike-slip regimes prevail with mainly left-lateral (sinistral) kinematics along SW-NE oriented lineaments, such as along the SEMP fault and the Mur-Mürz fault. Right-lateral (dextral) strike-slip, instead, occurs on NNW-SSE oriented lines, such as the Lavanttal fault, while to the north a compressional regime, with ~N-S oriented P-axes, is present.

4. GPS OBSERVATIONS AND ANALYSIS

4.1 Data and analysis

We analyze data from continuous GPS (cGPS) stations from several public and private networks, including both geophysical and non-geophysical networks, operating in the Euro-Mediterranean area. (see Fig. S6). The solution presented here is part of a wider Euro-Mediterranean geodetic solution, including >2000 cGPS stations that are analyzed in several sub-networks, and later tied together. The cGPS data-set in the study region is integrated with non-permanent observations coming from the semi-continuous OMBRA GPS network in the Montello area (Serpelloni and Cavaliere 2010; Danesi et al., 2015) for the 2009-2015 time-interval and from the Consortium for Central European GPS Geodynamic Reference Network (CEGRN) for the 1994-2007 time-interval (Fejes et al., 2006). GPS velocities have been obtained following a three-step procedure, as described in Serpelloni et al. (2006), which includes the

phase data reduction, the combination of regional and global solutions and the analysis of position time-series. More details on the GPS data processing and post-processing are provided in the supplementary material (Section S-2), and the reader is also referred to Serpelloni et al. (2013).

The GPS velocity field in Austria, Croatia and Slovenia is augmented by using additional geodetic solutions. In particular, our regional solutions have been combined with daily solutions, in the form of GAMIT hfiles, coming from the analysis of the CRODYN network in Croatia (Buble, 2012), and daily solutions of the Austrian GPS network (AMON), provided by OLGGPS (Mitterschiffthaler and Stangl, 2015; available at ftp:// olggps.oeaw.ac.at/pub/products/), in the form of Sinex files, for the 1998-2015 time-interval. For the latter dataset the original constraints in the solution files have been relaxed before the combination with our regional GAMIT solutions.

Because several unknown processes likely contribute to determine the continental-scale Common Mode Error (CME; see Section S-2 in the supplementary material), including the adoption of different models in the raw phase data processing, we do not filter out the CME from position time-series of stations derived from these two additional geodetic solutions, which results in larger uncertainties of the GPS sites present only in the two solutions.

The GPS velocities and uncertainties are reported in Table S3 of the supplementary material.

4.2 Velocity and strain-rate fields

The horizontal GPS velocities (shown in Fig.4) are used to estimate the strain-rate field adopting a multiscale approach (Tape et al. 2009). This method is based on a spherical wavelets approach that allows the estimation of a spatially continuous velocity field on a sphere starting from a set of irregularly spaced geodetic stations. The velocity value at a given point of the Earth's surface is obtained as a superposition of values obtained at different spatial scales, and then gradient quantities are directly derived from the estimated velocity field. The multiscale aspect is achieved by using wavelets from progressively finer meshes, which goes to finer scales only where justifiable, based on the GPS site density, that is allowing for short-scale spherical wavelets in the estimation where GPS stations are dense, and allowing only for long-scale spherical wavelets in the estimation where stations are sparse. The method locally matches the smallest resolved process according to the local spatial density of observations.

Using Tape et al., (2009) notation, q indicates the wavelet order with a corresponding spatial scale. In the case of tectonic deformation fields reasonable maximum values of q ranges

between 7 and 9, corresponding to scales of ~87 and ~22 km, respectively. The investigated area (Fig. 4) allows for minimum scale wavelets (q) equal to 3 (corresponding to a spatial scale of ~1390 km). We test different maximum values of q ($7 \leq q \leq 10$). With q_{max} greater than 9 (q = 10, corresponding to a spatial scale of ~11 km) only, spot-like areas are resolved at this scale (see Fig. S7). On the contrary, for almost all of the ESA of Italy and western Slovenia the geodetic strain rates are resolved at a spatial scale corresponding to a q_{max} = 9, that is the GPS network in the study area allows to resolve geodetic strain at a spatial scale smaller than ~22 km. Geodetic strain-rates in The Eastern Alps, north of the PAF, are resolved at a maximum spatial scale of ~44 km (q = 8), because the GPS network is less dense there.

Figure 4 shows horizontal velocities (white arrows) in a Eurasia-fixed frame, defined by a rotation pole located at Lon. -97.56±0.23°E, Lat. 55.99±0.25°N and rotating at 0.262±0.001 °/Myrs, superimposed on a map of the GPS speed (i.e., the scalar absolute value of the velocity) obtained using the multiscale method described above. In this work the Adria rotation pole (located at Lon. -28.24±0.79°E, Lat. 62.09±3.21°N and rotating at 0.508±0.006°/Myrs) has been estimated using cGPS sites in the Venetian (Veneto-Friuli) Plain and in the Istria peninsula, which is the only area of the Adriatic domains where northern Adriatic units outcrop. The Adria-Eurasia relative rotation pole is located at Lon. 8.17±1.21°E, Lat. 45.06±3.01°N and is rotating at 0.3253±0.0073 °/Myrs (Fig. 6a). Fig.4a shows the small circles (thin dashed line) around the geodetic pole of rotation (black star) showing the motion direction of Adria relative to Eurasia.

Overall our GPS velocity field is in agreement with previous results dealing with the broad kinematics of the eastern Alps and Carpathians (e.g., Grenerczy et al. 2005; Caporali et al., 2013; Cheloni et al., 2014; Metois et al., 2015), but is denser than previous ones in the southern Alps, Croatia and Slovenia. Fig. 4a shows that speeds >0.5 mm/yr (with site speed uncertainties ranging between 0.08-0.3 mm/yr) are present east of the Giudicarie lineament. Faster speeds (>2 mm/yr, shown in green, with site speed uncertainties ranging between 0.1-0.7 mm/yr) are present in the Adriatic area east of Lon. 12.5°E, including the Veneto-Friuli plain, western Slovenia and northern Croatia. The key features of the velocity field are *i*) the counterclockwise rotation of the Adriatic domain (including large part of Croatia) with respect to the Alpine mountain range and Europe, south of Lat. 46°N, with NNW-ward oriented velocities in the Venetian plain, increasing in speed from west to east, ii) the north-south velocity gradient with significant decrease in the geodetic speed across the southernmost front of the ESA in Italy and Slovenia and iii) the more east-ward component of motion of GPS stations north of the PAF (Fig. 4b), and east of Lon. 12.5°E. Fig. 4a highlights that across the ESA

front speeds decrease to values slower than 1 mm/yr, but do not go to zero in the ESA mountain core. In particular, GPS stations in the Dolomitic Alps move NW-ward at ~0.7 mm/yr (with site speed uncertainties ranging between 0.08-0.3 mm/yr), while sites in the Carnic Alps move N-ward at ~1 mm/yr (with site speed uncertainties ranging between 0.08-0.2 mm/yr).

Fig. 4b shows the discrete Eurasia-fixed velocities superimposed on a map of east component of the multiscale velocity field. Excluding the Emilia Po Plain, all the northern Adriatic area shows east-components close to zero, consistent with the general N-ward motion of the Adria microplate. Interestingly, in the ESA only the Montello-Cansiglio sector shows a non-zero eastward speed (at a rate of ~0.5 mm/yr, with site eastward velocity uncertainties ranging between 0.17-0.5 mm/yr). Positive eastward velocities are present north of the Fella-Sava and Periadriatic faults and east of the Žužemberk fault, with increasing E-ward rates toward the Sava folds. In particular, in the Eastern Alps positive E-ward velocities are ~0.5 mm/yr east of the Iseltal fault, and increase to values closer to 1 mm/yr east of the Lavanttal fault (with site eastward velocity uncertainties ranging between 0.1-0.3 mm/yr), and toward the Pannonian units. As already observed by Metois et al. (2015), GPS velocities (with respect to Eurasia) in the Alpine foreland (i.e., north of the Alpine front) do not go to zero but maintain an E-ward trend, which is however lower than in the Eastern Alps. Although out of the target area of this work, some kinematic features of the Alpine foreland are discussed in Section 5 and shown in Fig. S8.

All these features map into the multiscale strain-rate field, shown in Fig. 5, where the maximum compressional and extensional principal strain-rate axes are plotted on a regular grid and superimposed on a map of the scalar strain-rate values. Here the total strain-rate is taken as the Frobenius norm of the strain-rate tensor, defined as the square root of the sum of squares of all its components $|\dot{\epsilon}| = \sqrt{\dot{\varepsilon}_x^2 + \dot{\varepsilon}_{xy}^2 + \dot{\varepsilon}_{yx}^2 + \dot{\varepsilon}_{yy}^2}$ (Tape et al., 2009; Bos et al., 2003).

Relatively higher strain-rates (>0.15x10^{-7}yr^{-1}) are localized along a SW-NE oriented belt in Veneto and an E-W oriented belt in Friuli, corresponding to the southernmost ESA front, which continues to the east, in western Slovenia, approximately parallel to the Julian Alps thrust front and the Sava folds (see inset of Fig. 5). The highest geodetic strain-rates in the study area, as high as 0.36x10^{-7}yr^{-1}, are located in the Montello-Cansiglio region, with rates decreasing toward the east and toward the west. Lower strain rates with ~N-S oriented compressional axes, are present south of the Lessini Mountains, between the city of Verona and the Emilia Po Plain. Other secondary features (i.e., areas with lower strain-rate values) are discussed in Section 5.1.

Overall, the strain-rate field shown in Fig. 5 resembles the results from the Global Strain Rate Map project (GSRM; http://gsrm2.unavco.org; Kreemer et al., 2014), showing the belt of higher strain-rates running SW-NE along the ESA of Italy and E-W toward Slovenia, with comparable scalar strain-rate values. The differences, as for example in Istria where the GSRM model shows a concentration of higher strain-rates, likely arise from differences in the input GPS velocities.

The orientation of the principal strain-rate axes is in agreement with the orientation of the P-T axes obtained from the analysis of the FMs (see Fig. 5). In the ESA, between longitude 11°E and 13.5°E, the orientation of the maximum compressional strain-rate axes is consistent with the convergence direction predicted by the Adria-Eurasia rotation pole (see Fig. 5), with the exception of the Montello-Cansiglio area (between Lon. 12°E and 12.5°E). Here the azimuth of the maximum compressional strain-rate axes rotates counterclockwise with respect to the Adria-Eurasia convergence directions, forming an angle of ~10°, consistently with the P-axes orientation. Overall, principal strain-rate directions and P-axes are consistent with Adria-Eurasia convergence directions for the entire ESA belt, up to Lon. 15°E. In the Eastern Alps, despite the poorer resolution of the geodetic strain-rate field and the lower deformation rates, the orientation of the principal strain-rate axes is in agreement with the orientation of the P-T axes from earthquake FMs (Fig. 5). Secondary features of the strain-rate field (associated with lower strain-rates values, i.e., $< 0.2 \times 10^{-7} yr^{-1}$) are discussed in Section 5.1.

4.3 Velocities in different reference frames

In order to highlight secondary kinematic features that are not well mapped in the strain-rate field, because of smaller rates and sparser density of the GPS network, we define the horizontal velocities in different reference frames, and in particular with respect to the Adriatic micro-plate (Fig. 6a), the Dolomitic sector of the Southern Alps (Fig. 6b) and with respect to the Pannonian area (Fig. 6c).

Fig. 6a shows the overall southward motion of the Southern Alps with respect to the Emilia and Veneto-Friuli plains. The southward motion of the Lessini Mountains (LM) block and the city of Verona with respect to the Po Plain implies a N-S shortening of ~1 mm/yr, which is mapped in the strain-rate field (Fig. 5), but not well defined in its lateral spatial extent because of the sparse geodetic network in this sector of the Venetian plain. This N-S shortening is an important finding being possibly related to active thrusting south of the city of Verona, which can be tentatively associated with the large (Mw>6.5) 1117 Verona earthquake (see Fig. 2A). The source of this earthquake, which is the largest historical one in northern Italy is still debated

(e.g., Guidoboni et al., 2005; Galadini et al., 2001). These results, placing evidence for active shortening south of Verona, suggest a westward extension of the ESA thrust front south of the Lessini Mountains. The Lessini block, however, seems characterized by some minor internal deformation, and, although not directly measured by GPS data. A relative motion of this block with respect to Adria implies also a right-lateral motion along the Schio-Vicenza line, which is consistent with the observed tectonic regime from earthquake FMs (Fig. 3).

East of the Lessini Mountains, Fig. 6a shows a SSE-ward motion of the GPS stations located north of the southernmost ESA thrust front with respect to the Venetian plain. The highest velocities are located in the Montello and Cansiglio area (between longitude 12°E and 12.5°E, accordingly to the found high strain-rate values (Fig. 5) that decrease toward the SE and NE of this area. This segment of the ESA thrust front is the one showing. The direction of motion is about normal to the orientation of the thrust front but oblique with respect to the motion direction of Adria w.r.t. Eurasia, implying a left-lateral motion along SW-NE trending lineaments, in agreement with the observed strike-slip tectonic regimes in this area (Fig. 3). GPS sites south of the Bassano-Valdobbiadene thrust fault move faster than sites in the inner (dolomitic) Southalpine region, implying some NW-SE oriented extension, as mapped in the strain-rate field (Fig. 5), which is, however, not represented in the available FMs (Fig. 3).

East of the Cansiglio area fewer GPS sites sample the shortening across the ESA front. Fig. 6a shows that ~N-S shortening in the Friuli area is mainly accommodated across the Araba-Ragona and Susan-Tricesimo thrusts (~0.8 mm/yr) and the Gemona-Kobarid thrust (~1.1 mm/yr). Toward the east, Fig. 6a shows that right-lateral motion is accommodated along NW-SE oriented faults and ~N-S shortening is also accommodated across the Julian Alps thrust front, although GPS sampling here is poor. The prevailing tectonic regime in the Julian Alps is strike-slip (Fig. 3), with P-axes oriented consistently to the predicted Adria-Eurasia motion directions. GPS sites in the Friuli plain, near the city of Udine, display a SW-ward motion with respect to Adria, implying small (<0.5 mm/yr) shortening across the Pozzuolo-Medea (PT-MD) thrust faults, as also mapped in the strain-rate field (Fig. 5). This thrust system, which strikes parallel to Dinaric faults in northern Croatia and western Slovenia, crosscutting the E-W trending south alpine thrusts, shows evidence of Late Quaternary activity (Galadini et al., 2005), but the area is characterized by a low instrumental seismicity, and no historical earthquakes, or FMs, are associated with this structure. Further to the south, along the same strike of the Dinaric faults, SW-ward motion trends are present in northern Croatia, at sites confined between the Idrja and the Cicarija faults, implying ~0.5 mm/yr of shortening across the Cicarija segment of the external Dinaric thrust system, with respect to the stable (in an Adria-fixed

reference frame) Istria peninsula. This feature is consistent with the SSE-NNE oriented principal compressional strain-rate axes in this area (Fig. 5) and consistent with the tectonic regime from available FMs (Fig. 3). Fig. 6a shows that only limited constraints can be placed on the present-day activity ad kinematics of the major NW-SE trending Dinaric faults, i.e., the Raša and Idrja faults, due to the sparse geodetic network. Overall, considering the motion of GPS sites across the Idrja and Žužemberk faults a right-lateral motion can be inferred for these two faults, but how the general motion is accommodated at the two faults cannot be estimated with the available GPS network.

Fig. 6b shows GPS velocities with respect to a reference frame obtained by minimizing the velocities of sites located in the Dolomitic sector of the ESA (defined by a rotation pole located at Lon. -92.75±21.01°E, Lat. 56.53±18.62°N and rotating at 0.270±0.041 °/Myrs). In the Northern Giudicarie area, a few cGPS sites move toward the east, with respect to the Dolomites, implying some shortening (see also Fig. 5) in an area characterized by very low instrumental seismicity. In the central sector of the Venetian ESA, Fig. 6b highlights the NE-ward motion of the region confined between the Belluno-Valdobbiadene line (i.e., the pedemountain front) and the southernmost ESA thrust front (i.e., the Montello thrust). Overall, this region moves NE-ward with respect to the GPS stations located north of the Belluno-Valdobbiadene. Further to the north, Fig. 6b shows NNW-SSE oriented extension occurring between the Pedemountain front and the Belluno Valley and a weak signal of shortening across the Belluno and Valsugana lines, as mapped in the strain-rate field (Fig. 5). While no extensional focal solutions are present (see Fig. 3), strike-slip events are more frequent in this sector of the ESA, although it is not clear if strike-slip FMs are related to left-lateral motion along SW-NE oriented faults or to right-lateral motion along NW-SE oriented faults (see also Danesi et al., 2015). In the Carnic and Julian Alps Fig. 6b highlights a NE-ward motion of the Carnic (Friuli) Alps with respect to the Dolomitic Southern Alps. This relative motion would imply a left-lateral kinematics along N-S lineaments, which is possibly accommodated across the Fadalto line, where instrumental seismicity and strike-slip events are also recorded (Fig. 3), but its kinematics is not well constrained by near-fault GPS data. North of the Fadalto line no, or very little, seismic activity is present, but the area shows a great structural complexity (Castellarin et al., 2006). Considering the velocities of GPS sites in the ESA and in the Eastern Alps, our results confirm a small right-lateral motion across the PAF. However, Fig. 6b shows that ~0.7 mm/yr are taken up across the E-W trending Fella-Sava line, rather than along the Pusteri-Gailtal segment of the PAF, in agreement with one FM (Fig. 3). Right-lateral motion along the PAF is more apparent

moving eastward, in western Slovenia, where it is also better mapped by the available FMs (see Fig. 3).

Fig. 6c shows velocities in a reference frame obtained by minimizing the velocities of cGPS sites in the about aseismic Pannonian basin sector included in the study area (defined by a rotation pole located at Lon. -117.31±9.43°E, Lat. 38.11±26.5°N and rotating at 0.242±0.005 °/Myrs). This reference frame highlights an about E-W oriented extension between the Dolomitic and Carnic Southern Alps, as in Fig. 6b, which is not mapped by the available FMs (Fig. 3). Fig. 6c shows N-S shortening broadly accommodated across the Julian Alps thrust front and the Sava-Celje fault, consistent with orientation of the P-axes (Fig. 3). Across the triangular shaped region confined to the west by the Žužemberk fault, to the south by the Sava folds and to the north by the Sava-Celje line is a key area, a counterclockwise rotation of the velocity directions (from NNW to NE) occur, but it is not sufficiently sampled by GPS stations to provide indications about rates of deformation across the different faults or tectonic structures within this region.

In the Eastern Alps GPS velocities appear less coherent, limiting well-constrained kinematic inferences. An overall NNW-ward motion of GPS sites located north of the PAF and west of the Lavanttal line implies some relative motion between the Pannonian block and the Eastern Alps block. While FMs indicate right-lateral motion along this ~NS fault, the GPS data are less clear in defining its kinematics. The few GPS data across the Mur-Mürz fault indicate, consistently with FMs, a left-lateral kinematics for this fault, however, the few GPS sites across it prevent any more detailed kinematic analysis (see also Fig. S8). The kinematics of the Eastern Alps block (west of the Lavanttal fault) appears rather complex, with small rates and a few sites moving inconsistently. A general southward motion trend of sites between Lon. 12°E and 14°E, north of Lat. 46.5°N, imply some N-S shortening, which is also mapped in the strain-rate field (Fig. 5). Although not well determined, GPS velocities indicate a left-lateral motion across the SEMP and ISAM faults (see also Fig. S8).

5. KINEMATIC MODELING

In order to better constrain the main kinematic features highlighted by the GPS velocity and strain-rate fields and by the analysis of FMs, while providing a quantitative analysis of fault slip-rates, we use an elastic block modeling approach (e.g., McCaffrey, 2002; Meade and Loveless, 2009), representing the kinematics of the study area in terms of blocks motions and elastic (interseismic) strain accumulation at blocks-bounding faults. This approach allows

estimating relative rotation poles between block pairs and slip-rates from horizontal GPS velocities, assuming the geometry of blocks and blocks-bounding faults.

In this work we use the approach described in Meade and Loveless (2009), where blocks bounding faults are treated as freely slipping at the full relative plate motion below a given seismogenic depth above which they are either locked or partially slipping. In both cases the fault elastic contributions are calculated using the classical back-slip approach (Savage, 1983). We describe the results obtained using both planar rectangular dislocations (Okada, 1985), locked from the surface to a pre-defined locking depth value, and the results obtained using a curved surface, discretized by triangular dislocation elements, for the ESA thrust front, where the density of GPS sites is higher.

5.1 Blocks and Fault Geometries

The available catalogs of active faults, together with indications obtained from the analysis of the velocity and strain-rate fields and the map of seismic flux (Section 4), are used to define the blocks and faults geometries. Some constraints can be obtained from the geometry of seismogenic sources obtained from the analysis of macroseismic intensity data, as shown in the supplementary material. Fig. S2 shows seismogenic boxes, with confidence error ellipses, plotted together with FMs, with boxes in black characterized by constrained orientations. Dip angles and locking-depth values of blocks-bounding faults (assumed as planar rectangular dislocations) are defined from the Database of Individual Seismogenic Sources (DISS), Version 3.2.0 (DISS working group, 2015), the European Database of Seismogenic Faults (SHARE; Basili et al., 2013) and the analysis of crustal seismicity (see Section 3 and Figs S4 and S5). Fig. 7 and Fig. S9 show the final blocks and faults configuration. Dipping planes are used along the ESA front, the Dinaric faults in northern Croatia, and along the external front of the northern Apennines, with all other faults assumed as vertical dislocations. The elastic strains associated with fault perpendicular components of relative block motion across these vertical model faults are modeled using tensile dislocations.

As regard the ESA thrust front, east of the Schio-Vicenza line, in the Veneto and Friuli plains, it is represented by 10 segments with a dip of 40° and a locking-depth of 10 km. These values are both in agreement with the average values provided by the DISS, the distribution of instrumental seismicity (e.g., Danesi et al., 2015) and geological information (Galadini et al., 2005; Burrato et al., 2008). Our fault parameterization for the Thiene-Bassano and Montello segments differ from the DISS one. The absence of geodetic shortening between the stations VICE and SCHI (see Fig. 6 and Fig. S6), as opposed to the observed shortening between stations

CITD and BASS/MARO to the east, suggest that the westernmost segment of the Thiene-Bassano fault is shifted to the north, likely displaced by a NE-SW trending small transfer fault (the Valdastico line), in agreement with geological interpretations (e.g., Castellarin and Cantelli, 2000; Castellarin et al., 2006). As regard the western termination of the Montello thrust, the geometry the DISS includes a transfer fault offsetting the Thiene-Bassano and the Montello segments. The ~N-S orientation of this fault comes from the analysis of macroseismic data of the 1695 Asolo earthquake. However, as for the 1873 and 1936 Cansiglio earthquakes, the orientation of the 1695 seismogenic box is not reliable (see Table S2 and Fig. S2). Although small-size strike-slip events (Danesi et al., 2015; Fig. 3) may be consistent with the occurrence of right-lateral motion on NNW-SSE striking faults, the actual GPS network is not able to help discriminate between the presence of a transfer fault offsetting the southernmost Montello thrust from the Thiene-Bassano segment to the north, as proposed by Burrato et al. (2009), or the presence of a E-W trending lateral ramp of the main, arcuate Montello thrust system. We test the uniform-slip model considering both solutions (see Fig. S11) but develop the distributed-slip model assuming the presence of an E-W trending lateral ramp of the Montello frontal ramp.

While a boundary between the SALP and EALP blocks can be imagined by the analysis of GPS velocities (Fig. 6b) along the Fella-Sava fault, even if limitedly marked by seismicity, its NW-ward continuation is unclear, and here it is assumed to coincide with the westernmost segment of the Pusteri-Gailtal line. The link between these two segments is not clear and the area of transition from the Carnic Alps to the Dolomitic Alps is characterized by a complex structural setting (e.g., Castellarin and Cantelli, 2000), but the poor distribution and density of the GPS network and the lack of instrumental seismicity do not allow for more robust assumptions. As regard the boundary between the EALP and PANN blocks (Fig. 7) with stable Eurasia, as already discussed in Section 4, because of the slow rates and the scarcity of GPS sites across the Mur-Mürz and SEMP faults, the northern boundary of the EALP and PANN blocks is assumed to be located along the ISAM fault. However, regarding the Alpine foreland, as discussed in Section 4.2 and as already observed by Metois et al. (2015), GPS sites north of the Alpine front move toward the east at rates ≤0.5 mm/yr. In our model the ISAM fault represent the southern boundary of an Alpine foreland block, which is defined mainly by the analysis of GPS velocities, given the lack of clear seismicity lineaments. Fig. S8 shows that, in a Pannonian-fixed frame, left-lateral motion occurs between the PANN block and the Alpine foreland block (FORE in Fig. 7), the same for the EALP block. However, as shown by the two cross-sections in Fig. S8, where profile-normal velocities (showing lateral motion along ~EW lineaments) are

plotted, the slow rates and the sparser distribution of GPS stations prevent any detailed kinematic analysis (i.e., additional smaller blocks), justifying our simplified model where the ISAM fault is taken as the northern boundary of the EALP and PANN blocks. The kinematics of the Eastern Alps and of the Alpine foreland is likely more complex than the one imagined by our simple block model implementation, but modeling the slow deformation rates in the Alpine foreland is out of the scope of this work and in the following sections we discuss the model results mainly focusing on the ESA.

5.2 Model Results

Starting from Model 1 of Fig. S9, three additional models (Model 2, 3 and 4 of Fig. S9), with an increasing number of blocks in the ESA, have been tested, using the F-ratio test for additional plate boundaries (Stein and Gordon, 1984) to evaluate if more complex models are statistically significant or not. With respect to Model 1, Model 2 includes a Lessini Mountains block (LMNT), which accounts for observed kinematics in the Adria-fixed frame of Fig. 6a, as discussed in Section 5. Model 3 and Model 4 accounts for the observed different kinematics of GPS sites in the inner Dolomitic sector of the ESA and sites near the southernmost thrust front. In Model 3 the separation between the two Southern Alps blocks is placed along the Belluno-Valdobbiadene fault, and in Model 4 along the Valsugana fault.

The lowest residuals (reduced χ^2=8.7) are obtained for Model 2, where the addition of the Lessini Mountain block is justified by the F-ratio test. Models 3 and 4, instead, do not fit the observed velocities better, not justifying the need for additional blocks. Figure 7 shows the model geometry together with the observed and modeled velocities for Model 2 of Fig. S9. The model includes 479 GPS stations, with a mean residual magnitude of 0.4 mm/yr, and with 35% of stations having a residual velocity magnitude that is smaller than one standard deviation. The fact that reduced χ^2 value is much larger than 1 may be due to velocity uncertainty estimates that are too optimistic for sites with very long (>10 years) time-series, mainly in the stable Eurasian plate.

Velocity residuals from this model are shown in Fig. S10. Systematic SE-ward residual velocities are present in the Montello-Cansiglio segment of the ESA front, where the uniform slip model doesn't reproduce the clock-wise rotation of the velocity vectors at the GPS sites located between the southernmost thrust front and the Valsugana line. Models that include an additional block in the ESA (Model 3 and Model 4 of Fig. S9) do not better fit the measured velocities in this area.

Table S4 shows the rotation poles estimated for the blocks included in this analysis. Figure 8 shows the modeled slip-rates, both dip-slip or tensile (for vertical faults) and strike-slip components, as obtained for Model 2 of Figure S9. Overall, the modeled fault kinematics is in agreement with the seismotectonic data (Fig. 3), or geological information, when available, although for some sectors, as discussed in Section 6, slip-rate very close to 0 mm/yr and kinematic inconsistencies between close segments indicate poor constraints on blocks kinematics from the available GPS data. The discussion of the slip-rate values in the framework of the present-day knowledge is also discussed in Section 6.

5.3 Heterogeneous back-slip distribution along the ESA thrust front

Given the higher density of GPS sites and the presence of the systematic velocity residuals in the Montello-Cansiglio area (see Fig. S10), we develop a model where the ESA thrust front is discretized in triangular dislocation elements (TDEs), solving for spatially variable slip rates. A continuous surface has been realized starting from the rectangular planes defined in the model of Fig. 7 using the GMSH software (Geuzaine and Remacle, 2009). In particular, the ESA thrust front is discretized in 692 TDEs having an average area of ~5 km^2.

Using the approach of Loveless and Meade (2011), we invert for the distribution of back-slip, whose components are considered linearly independent from rotational blocks motion. Differently from other approaches (e.g., McCaffrey 2002), the method used allows also for forward slip, resolving, if possible, regions experiencing extremely low coupling or with ongoing very long period slow, or silent, slip events. The back-slip values are constrained to tape to zero at the fault bottom as representative bound of the brittle-ductile transition between upper and lower crust. The back-slip parameters' independence needs to be regularized to ensure continuity between adjacent fault elements and to modulate the back-slip values to be close to the values expected by projecting the relative blocks motion onto each TDE. This is ensured by imposing a smoothing constraint that minimizes the Laplacian of the slip along both strike- and dip- slip components (Meade and Loveless, 2009), which is weighted by a smoothing coefficient (β) controlling the extent to which TDE smoothness is enforced (e.g., Maerten et al., 2005). A small value of β permits a better fit to the GPS velocity data at the expense of an oscillating, physically unreasonable, TDE slip distribution, while a large β value strongly enforces smoothing such that back-slip on each TDE approaches a homogeneous value. Following Loveless and Meade (2016), β is defined as the value for which no more than 10% of TDE patches have a slip-rate that exceed the relative block motion rate,

which correspond to a β = 80. We calculate for each element of the fault surface the interseismic coupling (IC) coefficient by dividing the magnitude of back-slip rates by the magnitude of the slip-rate given by projecting relative block motions onto the TDE geometry.

Table S5 shows the rotation poles estimated for the blocks included in this analysis. Figure 9 shows the distribution of the dip-slip and strike-slip components of the coupling coefficient and of the resolution length (RL). The latter has been computed following Ader et al. (2012), and can be defined as the characteristic size of the smallest inhomogeneity of coupling that can be detected by the GPS network. To consider a spatial coupling feature as resolved, the RL should be constant on a fault and smaller than the coupling feature size itself (e.g., Anderlini et al., 2016). In general, the surface elastic signal caused by a TDE located at shallow depths has a short wavelength (few km) and can be potentially resolved only by a dense GPS network. A longer wavelength, detectable also by sparser networks, characterizes the signal associated with a deeper TDE.

As shown in Fig. 9, the ESA is characterized by prevailing inverse dip-slip components, in particular the Thiene-Bassano segment, the western ramp of the Montello thrust, the Polcenigo-Maniago and the Susans-Tricesimo segment, with slip-rate values all below 2 mm/yr. Two regions of forward slip (i.e., normal dip-slip rates) are present in correspondence of the Montello-Cansiglio thrust front, suggesting very low coupling in the dip-slip component. We find slow dip-slip rates for the Arba-Ragona segment. The strike-slip rates (Fig. 9b) are faster along the Montello and Polcenigo-Maniago segments, with right-lateral kinematics, as for the uniform slip model. Differently, for the Cansiglio segment the heterogeneous model predicts no to little strike-slip rates.

Allowing for heterogeneous slip on the ESA front results in a better fit to the GPS velocities, particularly for the Montello-Cansiglio segments, where motion directions shows a more E-ward oriented direction than surrounding sites. The heterogeneous model provides a limited improvement of the global reduced χ^2 value (=8.5) with respect to the uniform slip model. However, considering only the GPS sites located near the ESA thrust front, the improvement in the reduced χ^2 value is significant, passing from 5.1 to 3.6, and the root mean squared error from 0.3 to 0.2.

Fig. 9c shows the distribution of the interseismic coupling, highlighting three segments with relatively higher elastic coupling (i.e., the western ramp of the Montello thrust, the Polcenigo-Maniago and the Susans-Tricesimo segments), separated by regions with lower coupling degrees. Accordingly, to the distribution of GPS stations, the RL changes significantly along the ESA front (Fig. 9d). The RL increase to higher values (on average >25 km) down-dip,

being overall greater than 30 km below 10 km of depth. At shallower depths the RL is very long (on average >20 km) for the western ramp of the Montello thrust, suggesting that here variable interseismic slip is not resolvable at any spatial length smaller than the length of the segment itself. Moreover, because the GPS data are not sensitive to changes in the geometry of faults connecting the Thiene-Bassano and Montello thrusts (see Fig. S11), results for this segment are not reliable.

The Thiene-Bassano segment appears only partially coupled (IC ~0.5), in agreement with previous analyses (Cheloni et al., 2014), but the RL is on average ~10 km, which is about half of the length of this segment. The Montello frontal ramp results partially coupled (IC ~0.6) and characterized by a good resolution (RL < 10 km). The non-zero coupling is due to the higher strike-slip component of the back-slip distribution. The Cansiglio segment appears almost uncoupled (IC ~0.2), with RL on average <10 km. In Friuli, the Polcenigo-Maniago and Susans-Tricesimo segments appear mainly coupled down to ~10 of depth, but the RL along these segments is longer because of the scarce density of the GPS network. In particular, the RL is on average >15 km along the Polcenigo-Maniago segment, where no GPS sites are present across the thrust front, and >10 along the Susans-Tricesimo segment.

6. DISCUSSION

6.1 Kinematics and fault slip-rates: Eastern Southern Alps and Dinaric faults

The upper-left inset of Fig. 10a shows the traces of eight GPS velocity profiles conducted across the ESA front and the Dinaric and Slovenian deformation belts. For each cross section the observed GPS velocities, projected along or normal to the profiles, are plotted together with the velocities predicted by the block models (continuous and dashed lines in Fig. 10a and 10b), the swath topographic profiles and the distribution of seismicity (MRGC catalog) with depth.

Profile 1p extends from south to north across the Lessini Mountains block. The profile parallel components of the velocities show the ~1 mm/yr shortening accommodated between the Emilia Po Plain and the city of Verona. Here our model predicts dip-slip rates from 0.9 ± 0.2 to 2.1 ± 0.3 mm/yr, which are higher than the long-term slip-rates provided for the Verona source in the DISS, which are in the 0.1-0.5 mm/yr range. It is worth noting that the position and geometry of the N-ward dipping thrust fault in our model is largely unconstrained. Because of the lack of instrumental seismicity, the fault position has been located in between the region of geodetic shortening and its dip and locking depth values are

based on continuity with the other ESA thrust faults and information from the DISS and macroeismic information (see Fig. S2). Moreover, the Lessini Mountains block is undergoing some additional, slow rate, internal deformation, partially highlighted by the few FMs and the instrumental seismicity indicating activity of the NW-SE oriented faults. Additional investigations, including an improvement of the geodetic network, will be necessary to better constrain the kinematics of this area, which has been hit by one of the largest historical earthquake of the study region, the Mw~6.6, 1117 Verona earthquake.

The Schio-Vicenza line transfers the Adria-Alps shortening from the Verona segment of the ESA front to the Thiene-Bassano segment, with a left-lateral slip-rate of 0.4 ± 0.2 mm/yr in the Venetian plain. Its northern segment (i.e., in the Alpine domain), accordingly to the available FMs, accommodates a right-lateral motion with a slip-rate of 1.0 ± 0.1 mm/yr.

Profile 2p defines a transect perpendicular to the Thiene-Bassano segment of the ESA front, where the profile parallel components of velocities show the ~1 mm/yr of shortening occurring across it. The dip-slip rate estimated for this segment is of 1.5 ± 0.1 mm/yr, which is higher than the upper bound placed in the DISS of 1 mm/yr. It is worth noting that the heterogeneous and uniform slip models fit almost equally well the observations, and in order to put further constraints on the estimated low interseismic coupling for this thrust fault additional GPS sites will be necessary.

Profile 3p defines a transect perpendicular to the Montello segment of the ESA thrust front, where ~1 mm/yr of shortening is accommodated within ~10 km of the fault trace, as indicated by a sharp velocity gradient across the Montello hill. The uniform-slip model provides a dip-slip rate of 1.6 ± 0.1 mm/yr but a poor fit to the data (see the dashed line in Profile 3p of Fig. 10a). This slip-rate value is comparable with geological estimates from Benedetti et al. (2000), who provided a long-term slip rate of 1.8-2 mm/yr, and with the upper bound provided in the DISS (i.e., 1.56 mm/yr). It is worth noting that the DISS includes an additional seismogenic source, the Bassano-Valdobbiadene thrust, placed north of the Montello thrust, after Barba et al. (2013), who modeled geodetic (i.e., leveling) vertical rates across this sector of the ESA thrust front. Models that include additional thrusts faults north of the Montello fault (see Mod3 and Mod4 in Fig. S9) are not statistically justified, and do not better fit the data. The heterogeneous slip model provides a better fit to the measured GPS velocities (see the continuous line in Profile 3p of Fig. 10a), although the observed shortening between MT01 and MT02 stations is still higher than predictions. The variable slip model provides a higher strike-slip (left-lateral) slip-rate than the uniform slip one, but also suggests the occurrence of

forward (i.e., normal) dip-slip motion (see Fig. 9a), thus a limited interseismic coupling for the Montello segment (see Fig. 9c).

For the Cansiglio segment of the ESA front the uniform-slip model provides a dip-slip rate of 1.4±0.1 mm/yr and a strike-slip rate of 0.5±0.1 mm/yr, which accommodates the ~1 mm/yr of left-lateral motion observed across this sector (see Profile 4n, showing profile perpendicular components of velocity). The estimated slip-rate is higher than the values provided in the DISS, whose upper bound value is of 0.8 mm/yr. The heterogeneous slip model (Fig. 9), as for the Montello thrust, suggests that this segment of the ESA front is mostly creeping aseismically, but the near-field GPS sampling here is poorer than across the Montello segment (see continuous line in Profile 4p of Fig. 10a).

It is worth noting that GPS velocities across the Montello and Cansiglio faults (Fig. S10) are characterized by a similar orientation of the model residuals. A few sites located on the pedemountain chain (see orange symbols in Fig. 10a), in the hangingwall of the two faults, show, in fact, higher residuals with respect to model predictions. In particular, the residual motions of these sites are oriented S-SE-ward (see Fig. 9c), and their measured motion would suggest a NNW-SSE oriented extension, as also shown in the Profiles 3p and 4p of Fig. 10a, which is difficult to explain in a convergence tectonic setting. This behavior is not explained by more complex models, as discusses in Section 5.1, and is better, but still partially, explained by a forward (i.e., normal) slip motion on these two segments giving the low interseismic coupling values. A possible explanation for these systematic residuals is that here the GPS sites are not properly measuring the long-term linear motion rates, possibly due to transient deformation (e.g., Loveless and Meade, 2010). The occurrence of hydrological-induced, time-variable, deformation in the Alpago-Cansiglio has been described by Devoti et al. (2015) from the analysis of GPS time-series. This deformation signal, which is larger in the horizontal components, correlates with rainfall measurements and it has been explained as due to fluid circulation in the karst rocks of the area. Importantly, the direction of motion of GPS sites of the hydrological-induced deformation is oriented toward the SE, accordingly to the direction of the model residuals. We speculate that these hydrological-induced deformations may be extended to the entire pedemountain chain, which is characterized by karst rocks.

The ~N-S Profile 5p in Fig. 10a is conducted across the E-W Araba-Ragona segment of the Friuli ESA thrust front, the Fella-Sava and the PAF Pusteri-Gaital lines. Overall, ~2 mm/yr of N-S shortening are accommodated in this area. The uniform-slip model provides 1.6±0.1 mm/yr of dip-slip rate but here the heterogeneous slip-model is unconstrained due to the scarce density of the GPS network across the mountain front, where the uniform-slip and

heterogeneous-slip models equally fit the measured velocities (see the dashed and continuous lines in Fig. 10a). The estimated dip-slip rate for the Araba-Ragona fault is higher than the slip-rate values provided by the DISS that gives an upper bound of 0.3 mm/yr but assuming that shortening in the Friuli segment of the ESA thrust front is accommodated through up to three sub-parallel thrust faults, each having an upper bound slip-rate of 0.5 mm/yr. For the Friuli sector of the ESA front D'Agostino et al. (2005) estimated a slip-rate of 2.4 mm/yr, which is also higher than our estimate, but tis value has been obtained modeling the observed N-S shortening using a single thrust-fault accommodating all the deformation from Italy to Austria, whereas our model includes more faults north of the ESA thrust front. In particular, north of the Araba-Ragona fault the observed velocities are explained including shortening to be accommodated across the Fella-Sava fault (with a tensile-rate of 0.7 ± 0.1 to 0.9 ± 0.1 mm/yr), which also accommodates right-lateral motion (see Fig.6), as shown in Profile 5n of Fig. 10a, and for which a strike-slip rate of 1.1 ± 0.1 to 1.2 ± 0.1 mm/yr is estimated. The SHARE database, which extends the DISS outside Italy, includes both the Fella-Sava and Periadriatic faults for which it provides slip-rates of 0.15 and 1 mm/yr (as upper bounds), respectively. Our model, on the contrary, mainly justified by the measured GPS velocities (see Section 4.3), includes only the Fella-Sava, and the estimated slip-rate is in agreement with the SHARE upper bound value for the PAF.

Profile 6 of Fig. 10b defines a transect perpendicular to the Susans-Tricesimo segment of the ESA front, where ~1 mm/yr of shortening is accommodated. The uniform-slip model (with 1.3±0.1 dip-slip rate and 0.8±0.1 right-lateral strike-slip rate) and the heterogeneous slip one equally fit the measured profile parallel and profile-normal velocities (see Fig 10b), with the latter suggesting that this segment is mainly coupled. Profile 6n shows how our model fits the right-lateral motion observed across the Susans-Tricesimo and the Fella-Sava faults.

Cheloni et al. (2014) analyzed the distribution of the interseismic coupling along the ESA thrust front using an approach similar to the one used in this work, constraining the coupling coefficient to be confined between 0 and 1. Our fault model differs both in the dip of the thrust system, which is assumed here as dipping 40° to the north, whereas Cheloni et al. (2014) model the thrust front using a N-ward 30° dipping surface, and in the depth, being our model limited to the first 15 km of depth, depicting the frontal ramp of the ESA thrust system. Overall, our model fits the GPS velocities in the ESA better than Cheloni et al.'s (2014) model, and GPS data are denser in its Venetian sector, particularly in the Montello and Cansiglio area. As in Cheloni et al. (2014), the Susans-Tricesimo segment appears mainly coupled down to ~10 km of depth. For the Araba-Ragona and Polcenigo-Maniago segments, because of the poor GPS networks

density, the current data doesn't allow to significantly distinguish between a uniform-slip or a heterogeneous-slip model, although Fig. 9 shows that, accordingly to Cheloni et al. (2014), the Polcenigo-Maniago segment appears interseismically coupled. For the Veneto sector of the ESA thrust front (i.e., the Thiene-Bassano, Montello and Cansiglio segments) our results someway agree with Cheloni et al. (2014) results that suggest a more limited coupling for these faults. For the western ramp of the Montello thrust, as discussed in Section 5, the results for this segment are unconstrained.

Profile 7 in Fig. 10b is drawn perpendicular to the Dinaric faults in Croatia and Slovenia, intersecting to the Sava-Celje and Lavanttal faults. The profile parallel velocities (Profile 7p) show that ~1 mm/yr of NE-SW shortening is accommodated across the Dinaric fault in Istria and Slovenia. In particular, the model dip-slip rate for the Raša fault is 1.0 ± 0.2 mm/yr. The poor GPS coverage in this area doesn't allow further constraints on activity of more external thrust faults, like the Cicarija thrust. Between the Raša and the Žužemberk faults the few GPS stations suggest that there is no shortening going on, which is instead accommodated across the Sava folds and Sava line area. Profile 7n in Fig. 10b shows that ~1.2 mm/yr of right-lateral motion are accommodated across the Dinaric faults and ~1 mm/yr across the Sava and Celje faults. While the Raša, Idrja and Žužemberk faults appears seismically active, the lack of a dense GPS network in this area doesn't allow further constraints on the way the observed right-lateral motion is partitioned among these three major structures. Our model provides a right-lateral strike-slip rate of 0.7±0.4 mm/yr for the northern segment of the Žužemberk fault, which is faster (up to 1.7±0.4 mm/yr) in its southern segment) and of 1.4±0.1 and 1.0±0.3 mm/yr for the Sava and Celje faults, respectively. Moulin et al. (2014), based on morphotectonic analyses, provides a lower-bound long-term slip-rate of 1.5 mm/yr for the Idrja fault, which is much higher that the block model estimate for the Žužemberk fault, assuming that the observed ~1.2 mm/yr of right-lateral across the Dinaric faults is likely to be partitioned onto more sub-parallel faults. The model slip-rate, on the contrary, is similar to the values assigned to the Dinaric faults in the SHARE database, which mostly come from Kastelic et al. (2012, 2013) and finite element modeling of the Dinaric area. Constraints on the activity and slip-rates in this area are certainly limited by the poor GPS stations coverage, but the available stations pose an upper bound value of ~1.2 mm/yr for the right-lateral motion accommodated on the NW-SE striking Dinaric faults (see Profile 7n in Fig. 10b).

Profile 8 of Fig. 10b crosses the triangular-shaped zone encompassing the Sava folds and Sava-Celje fault system. Profile parallel components of velocity (Profile 8p) show the ~2 mm/yr of N-S shortening occurring across this distributed zone of deformation. While for the southern

boundary of this area (i.e., the Sava folds boundary) the model provides not well constrained tensile rates for its northern boundary, i.e. the Sava and Celje fault, the model provides tensile (compressional) rates of 1.2±0.4 and 0.7±0.3 mm/yr, respectively. It is worth noting that given the distribution of GPS stations any further constrain on the way this shortening is partitioned across different sub-parallel structures is prevented. Nevertheless, it is clear that this area plays an important role in accommodating both the N-S shortening due to Adria and Dinaric units motion (with respect to the south Alpine area), and the E-ward motion of the Pannonian units. This complex deformation is likely distributed rather than accommodated by a single fault and a better understanding will require a denser GPS network. The SHARE database suggests the activity of several sub-parallel smaller faults, mainly N-verging, for the Sava fold area, with upper-bounds slip-rates of 0.2 mm/yr. Profile 8n in Fig. 10b shows the right-lateral motion (~1 mm/yr) accommodated across the western boundary of the Sava block with a slip-rate of 1.7 mm/yr, which is however not well constrained because of lack of GPS stations in inner Croatia. To the north, profile 8n shows the left-lateral motion accommodated along the Sava folds area, for which a slip-rate of 3.3±0.5 mm/yr, likely accommodated on different sub-faults, is estimated.

6.2 Kinematics and fault slip-rates: Eastern Alps

Kinematics and crustal deformation in the Eastern Alps and the western Pannonian basin included in our study area are less constrained than the ESA, due a sparser GPS network, slower deformation rate and relatively larger variability in the motion trends. Our simplified model for the Eastern Alps include two blocks (EALP and PANN), which have been defined from available faults databases and geodetic velocities. While the kinematics of the southern boundaries of the Eastern Alps blocks are rather well constrained by the available data, running from west to east along the Periadriatic, Fella-Sava and Celje faults, the northern boundaries are less constrained.

The activity and kinematics of the Mur-Mürz fault is rather well imaged by earthquake FMs, indicating left-lateral strike slip on WSW-ENE lineaments. However, as shown in Fig. S8, the scarcity of GPS sites across it prevent any more detailed analysis, at least with the block modeling approach used. The activity of the SEMP fault is less constrained by seismotectonic indicators, but as for the Mur-Mürz fault the low deformation rates, a complex kinematics (see Fig. S8) and a sparser GPS network prevent a better-constrained analysis of the slip-rates. The model predicts a left-lateral strike slip-rate of 0.3±0.1 mm/yr for the SEMP fault bounding to

the north the PANN block (slower than the upper-bound slip-rate in the SHARE database, of 1 mm/yr), while for the northern boundary of the EALP block the model slip-rate is close to zero.

The relative motion between the EALP and CALP blocks (Fig. 7) implies a right-lateral trans-tensional motion across the Brenner fault, with slip-rates that are in agreement with upper-bound rates in the SHARE database. The relative motion of the EALP and PANN blocks, as suggested by earthquake FMs, is accommodated along a complex tectonic structure that is simplified in our model using a linear (vertical) fault roughly corresponding to the Lavanttal fault. For this fault the model provides a right-lateral, transpressive, motion with a strike-slip slip-rate of 0.5±0.1 mm/yr, which is within the range provided in the SHARE database.

6.3 Seismic potential along the Eastern Southern Alps deformation belt

The analysis of the seismic moment release (Fig. 3) and of the geodetic strain (Fig. 5) highlights a belt where both rates are higher. The area corresponds to the region characterized by the highest seismic hazard of the great Alpine region (Giardini et al., 2014), and includes the WSE-ENE trending ESA thrust front and its E-W eastern continuation through Friuli and Slovenia (see upper-right inset in Fig. 5). For this area we compare the seismic moment rates (i.e., given here in terms of seismic flux) and the geodetic moment rates (converted in geodetic seismic flux).

Fig. 11 shows the geodetic and seismic flux values plotted as a function of distance along two profiles (A-B and C-D in the two insets of Fig. 11) running parallel to the two segments of the ESA deformation belt. The colored lines show the maximum value of all quantities within the swath profiler. The figure shows the seismic flux obtained from 1005, 1600 and 1900 (blue, grey and black lines, respectively) and the Mw≥5 earthquakes occurred within the swath profile, plotted as a function of time from 1005. The geodetic flux is computed from the strain-rates (red lines in Fig. 11) obtained from the velocities calculated on a regular grid using the results from the model including variable coupling on the ESA thrust front. The geodetic flux for each 0.1°x0.1° grid cell is calculated using the scalar version of the Kostrov's formula (Kostrov, 1974), using as scalar value of the geodetic strain-rate the total strain-rate defined in Section 4.2, a rigidity modulus of 30×10^9 N/m^2, considering both the depth of the upper crust from the EPCRUST model and the depth of the seismogenic layer estimated from the distribution of earthquakes (see Fig. S4). The geodetic flux can be considered as the upper bound of the accumulation rates of seismic moment (per unit area) as measured by GPS data and elastic earthquake cycle modeling. The geodetic flux calculated using the upper crust (UPC) depth is on average 1.4% higher than the geodetic flux calculated using the seismogenic

layer depths, and, in general, using the UPC depth provides a positive gap between the geodetic flux and the seismic flux calculated using the whole seismic catalogue time span.

Profile A-B in Fig. 11 shows that along the Veneto-Friuli ESA mountain front the geodetic strain rate and the seismic flux calculated from 1600 and 1900 increase toward the east following similar trends. In the western sector of the profile (i.e., west of the Asolo segment) the seismic flux calculated from 1600 and 1900 is lower that the geodetic flux. This segment, which includes the Venetian plain south of the Lessini Mountains and part of it, is characterized by infrequent instrumental and historical seismicity. The single Mw>6.5 event occurred in 1117 near Verona fills the gap between the geodetic and seismic flux, suggesting that this area is likely characterized by large earthquakes (possibly with long return times), even larger or of comparable size than earthquakes occurred in the fastest deforming segments of the ESA front, releasing the strain accumulated at relatively lower rates. The eastern Lessini and the Thiene-Bassano segments of profile A-B, on the contrary, show a large gap between the geodetic and seismic flux values, considering the three time intervals. This can be due to real low seismicity rates and incomplete information on historical earthquakes or to the way these regions release the accumulated deformation. For the eastern Lessini area, where a lowering of both the strain-rate and the geodetic flux is present, the current kinematics is likely more complex than accounted in our model. This area, in fact, transfers the ESA thrust front from the Verona segment to the north through smaller faults, including NW-SE oriented strike-slip faults, belonging to the Schio-Vicenza system, and smaller E-W thrusts (e.g., Castellarin and Cantelli, 2000; Viganò et al., 2008). As regard the Thiene-Bassano segment, where no Mw>5 earthquakes occurred from 1005, the analysis of variable interseismic coupling (Fig. 9) would suggest a partial coupling for this segment, implying some aseismic deformation, but here the coupling analysis is not well constrained by the limited number of GPS sites.

East of the Thiene-Bassano segment both the geodetic strain rates and the seismic flux increase, together with the number of Mw>5 earthquakes from 1600. The highest geodetic strain-rates correspond to the Montello thrust, whereas relatively lower strain rates are present for the Asolo and Cansiglio segments. For the latter segments, the seismic flux values are similar to the geodetic flux ones, calculated from 1600 and 1900. For the Asolo segment, however, the GPS network doesn't allow putting constraints on the fault geometry and interseismic coupling (as discussed in Section 5.3). For the Montello fault, the presence of high geodetic strain-rates, low seismic flux and low interseismic coupling (Fig. 9) suggest that this segment of the ESA thrust front is most likely releasing large part of the accumulated deformation aseismically. Also the Cansiglio thrust segment shows limited interseismic

coupling (Fig. 9), but here the value of the seismic and geodetic flux is similar. It is worth noting that the A-B profile samples also the inner mountain front north of the Cansiglio plateau, where larger earthquakes, most likely associated to ~N-S strike-slip faults, are present.

The profile C-D in Fig. 11 runs parallel to the Friuli and Slovenian ESA front, through the Carnic, Julian and Kamnik Alps. As for the profile A-B, the geodetic strain-rates and the seismic flux follows similar trends, lowering toward the east. The Friuli segment (i.e. Carnic Alps in Fig. 11) is characterized by recent Mw>5 seismicity (mainly associated to the Friuli seismic sequence started in 1976). Here the seismic flux calculated from 1600 and 1005 are consistent with the geodetic flux. On the contrary, the seismic flux from 1900 is higher than the geodetic flux, which can be due to the recent high seismicity rate and the time interval that is too short to estimate a reliable seismic flux.

Toward the east, Fig. 11 shows the only segment of the ESA front where the seismic flux calculated from 1000 is higher than the geodetic flux. Here the greatest contribution to the seismic flux comes from 1511 (Mw~6.9) event, and a possible explanation for this discrepancy is an overestimation of the equivalent moment magnitude of this historical event. The Julian Alps, where N-S shortening is still going-on (Fig. 5) along the Julian Alps Thrust front (but al lower rates than surrounding segments), there is a gap between the seismic and geodetic flux. This gap can be interpreted as a seismic gap in the ESA southern front, with respect to its segments in Friuli and in the Kamnik Alps, both characterized by larger and more frequent earthquakes from 1005. However, here the geodetic strain-rates and kinematics are not well constrained by the GPS network and this area is characterized by a complex structural setting caused by the interaction between the E-W ESA thrust front and the NW-SE trending Dinaric faults, which may result in smaller magnitude earthquakes than in the Friuli and Veneto ESA segments. Further to the east, in the Kamnik Alps segment of profile C-D of Fig. 11 the gap between the geodetic and seismic flux is smaller (if computed from 1005) or null (if computed from 1600) than in the Julian Alps segment of the profile. It is worth noting that for this area the historical seismic catalogue can be considered complete for Mw>5.8 earthquakes starting from 1850, being complete from 1500 in the rest of the Alpine area (Stucchi et al., 2012), so explaining the differences in the seismic and geodetic flux values for the eastern sector of the C-D profile of Fig, 11 is more complicated by our more limited knowledge of the seismic history.

7. CONCLUSIONS

Fig. 12 highlights some of the main findings of this study. The greater part of the northern Adriatic region is moving consistently with the Adriatic microplate (areas in red in

Fig. 12). In particular, the northern Dinaric area (area in light red in Fig. 12) presents small residual motions with respect to Adria, indicating limited shortening across the NW-SE trending Dinaric faults in northern Slovenia and Croatia, and providing an upper bound value (1.2 mm/yr) of the right-lateral motion between stable Adria and the Pannonian block.

The larger part of the Adria-Eurasia convergence is accommodated across the southernmost ESA thrust front, where the highest geodetic strain-rates are observed in the central segment of the Venetian ESA front (the Montello and Cansiglio thrusts), with rates decreasing toward the west and the east. The western continuation of the Venetian ESA runs south of the city of Verona, locus of one of the larger historical earthquake of the study area, where N-S shortening is associated to the S-ward motion of the Lessini Mountains block with respect to the Adriatic microplate. The continuation of the ESA front in Slovenia is more uncertain. N-S shortening continues along the Julian Alps thrust front, but here deformation is more distributed and complex than in the Italian ESA front.

The analysis of interseismic coupling in the Veneto-Friuli sector of the ESA thrust front, although it is not uniformly resolved, reveals segments that are mostly locked, like in the Friuli ESA, and segments with lower coupling values, such as the Montello and Cansiglio ones. Here GPS velocities highlight more E-ward oriented velocities that rotate N-ward north of the mountain front, that are only partially explained by the variable slip model. The area between the ESA thrust front and the PAF (light blue areas in Fig. 12) move still N-ward at lower rates. We highlighted a relative motion between the Dolomitic and Carnic sectors of the ESA, implying a left-lateral motion along N-S lineaments (like the Fadalto line) and a E-W extension, which are however explained by the elastic block model without the need of adding additional blocks in the ESA area.

The Eastern Alps (green areas in Fig. 12) shows E-ward rates slightly increasing toward the Pannonian basin, east of the Levantall fault. The right-lateral motion between the ESA and EA blocks is largely accommodated by the Fella-Sava fault, rather than the Periadriatic fault (PAF). However, the kinematics of the PAF is less constrained both W and E of the Fella-Sava. In Slovenia, in particular, because of the lower density of the GPS network, the role of the PAF with respect to the Sava and Celje faults in accommodating right-lateral motion is not clear. In our interpretation, however, the Fella-Sava and Žužemberk faults represent a major tectonic lineament, separating a domain moving consistently with the Adria microplate (red and blue areas in Fig. 12) from a domain moving more E-ward (green areas in Fig. 12). In this framework, the triangular-shaped zone encompassing the Sava-Celje faults and the Sava folds plays a major role in accommodating the transition from the Adriatic to the Pannonian-Balkans domains.

Here seismotectonic and GPS data suggest the occurrence of a distributed deformation where N-S shortening is still the dominating geodetic deformation signal.

The kinematics of the northern boundaries of the EA blocks are more uncertain, due to the slow motion rates and the sparser GPS network. GPS data indicate a slow (< 0.5 mm/yr) E-ward motion of the Alpine foreland with respect to stable Europe, and a left-lateral motion between the EA blocks and the Alpine foreland that is accommodated by several faults, including the Mur-Mürz, SEMP and ISAM faults. However, the sparser GPS network doesn't allow further constraints on geodetic slip-rates. Moreover, the EA block confined between the Brenner and Levantall faults is likely characterized by a more complex kinematics, as also shown by the available FMs.

We estimated the seismic flux (moment release rate per unit area) from the integrated seismic catalogue and the geodetic flux (moment accumulation rate per unit area) from the model geodetic strain-rate field, and compare these quantities along the ESA front of Italy and Slovenia. Despite the known limitations of historical and instrumental earthquake catalogs in slowly deforming regions (e.g., uncertainties in the location and magnitude, incomplete instrumental and historical seismicity) and the uncertainties on the seismogenic layer (largely affecting the geodetic flux estimates), this analysis provided new insights into the seismic potential of this area. While small positive or negative gaps can be due to the intrinsic uncertainties and limitations of the methods, larger gaps bring information on the seismic potential or dealing with the earthquake catalogue (e.g., incompleteness or overestimation of the magnitude). While the seismic flux calculated from 1005 (i.e., the longer time span of our analyses) is close to the upper bound values provided by the geodetic flux along large part of the ESA front, reliable constraints on the seismic potential come where the state of interseismic coupling is known with a higher degree of confidence. This is the case of the Montello thrust, where high strain-rates, low seismic flux values and lower interseismic coupling suggest that part of the geodetic strain is released aseismically.

In the eastern sector of the European Alps the kinematic indicators derived from seismological and geodetic data are remarkably consistent at different spatial scales. Although the overall kinematics was known, several kinematic features bringing important implications for the evaluation of the seismic hazard and the dynamics of continental collision have been highlighted in this work, demonstrating both the fundamental role of regional GPS networks densified across active faults and the integration of geodetic and seismological observations. Nevertheless, several sectors of the study area require more GPS stations and more detailed studies of instrumental and historical seismicity.

Acknowledgments

We thank the editor, Philippe Agard, and two anonymous reviewers for their constructive comments. We are grateful to all public and private institutions that made the continuous GPS data used in this work available. We thank the State Geodetic Administration of the Republic of Croatia and Faculty of Geodesy, University of Zagreb for making available GPS data and solutions of the CRODYN project. This study has been partially funded by the Italian Presidenza del Consiglio dei Ministri, Dipartimento di Protezione Civile (Proj. S1 2013-2014 INGV- DPC Agreement). This paper does not necessarily represent an official opinion or policy of the Dipartimento di Protezione Civile. Letizia Anderlini has been supported by Progetto "PREMIALE 2011: Studio multidisciplinare della fase di preparazione di un terremoto." We thank John P. Loveless and Brendan J. Meade for their help with the block-modeling code and Carl Tape for making available his strain rate estimation code. We thank Romano Camassi and Filippo Bernardini for helpful discussions on the historical seismicity and Adriano Cavaliere for field support in the maintenance of the OMBRA GPS network. All figures have been made using the GMT software (Wessel et al., 2013).

References

Ader, T., Avouac, J.-P., Liu-Zeng, J., Lyon-Caen, H., Bollinger, L., Galetzka, J., Genrich, J., Thomas, M., Chanard, K., Sapkota, S.N., Rajaure, S., Shrestha, P., Ding, L., Flouzat, M., 2012. Convergence rate across the Nepal Himalaya and interseismic coupling on the Main Himalayan Thrust: Implications for seismic hazard. J Geophys Res 117. doi:10.1029/2011JB009071.

Aktug, B., Nocquet, J.M., Cingoez, A., Parsons, B., Erkan, Y., England, P., Lenk, O., Guerdal, M.A., Kilicoglu, A., Akdeniz, H., Tekguel, A., 2009. Deformation of western Turkey from a combination of permanent and campaign GPS data: Limits to block-like behavior. J Geophys Res 114. doi:10.1029/2008JB006000.

Anderlini, L., E. Serpelloni and M.E. Belardinelli, 2016. Creep and locking of a low-angle normal fault: Insights from the Altotiberina fault in the Northern Apennines (Italy), *Geophys. Res. Lett.*, 43, 4321–4329; doi:10.1002/2016GL068604.

Barba, S., Finocchio, D., Sikdar, E., Burrato, P., 2013. Modelling the interseismic deformation of a thrust system: seismogenic potential of the Southern Alps. Terra Nova.

Basili R., Kastelic V., Demircioglu M. B., Garcia Moreno D., Nemser E. S., Petricca P., Sboras S. P., Besana-Ostman G. M., Cabral J., Camelbeeck T., Caputo R., Danciu L., Domac H., Fonseca J.,

García-Mayordomo J., Giardini D., Glavatovic B., Gulen L., Ince Y., Pavlides S., Sesetyan K., Tarabusi G., Tiberti M. M., Utkucu M., Valensise G., Vanneste K., Vilanova S., Wössner J. (2013). The European Database of Seismogenic Faults (EDSF) compiled in the framework of the Project SHARE. *http://diss.rm.ingv.it/share-edsf/*, doi: 10.6092/INGV.IT-SHARE-EDSF.

Battaglia, M., Murray, M.H., Serpelloni, E., Bürgmann, R., 2004. The Adriatic region: An independent microplate within the Africa- Eurasia collision zone. Geophys. Res. Lett. 31. doi:10.1029/2004GL019723.

Bechtold, M., Battaglia, M., Tanner, D.C., Zuliani, D., 2009. Constraints on the active tectonics of the Friuli/NW Slovenia area from CGPS measurements and three-dimensional kinematic modeling. J Geophys Res 114. doi:10.1029/2008JB005638.

Benedetti, L., Tapponnier, P., King, G., Meyer, B., Manighetti, I., 2000. Growth folding and active thrusting in the Montello region, Veneto, northern Italy. J Geophys Res-Sol Ea 105, 739–766.

Bertotti, G., Picotti, V., Bernoulli, D., Castellarin, A., 1993. From rifting to drifting: tectonic evolution of the South-Alpine upper crust from the Triassic to the Early Cretaceous. Sediment. Geol. 86, 53–76.

Bilham, R., 2013. Societal and observational problems in earthquake risk assessments and their delivery to those most at risk. Tectonophysics 584, 166–173. doi:10.1016/j.tecto.2012.03.023.

Bos, A. G., Spakman, W. and Nyst, M.C.J., 2003. Surface deformation and tectonic setting of Taiwan inferred from a GPS velocity field, J. Geophys. Res., 108(B10), 2458, doi:10.1029/2002JB002336.

Braunmiller, J., Kradolfer, U., Baer, M. and Giardini, D. (2002). Regional moment tensor determination in the European-Mediterranean area - initial results, Tectonophysics 356, 5-22.

Bressan, G., Bragato, P.L., Venturini, C., 2003. Stress and Strain Tensors Based on Focal Mechanisms in the Seismotectonic Framework of the Friuli–Venezia Giulia Region (Northeastern Italy). Bulletin of the Seismological Society of America 93, 1280–1297. doi:10.1785/0120020058.

Buble, G., 2012. Microplate kinematics, intraplate deformation and sea level rise in Europe. Ph.D. 238 p. (http://arizona.openrepository.com/arizona/handle/10150/223374).

Burrato, P., Poli, M.E., Vannoli, P., Zanferrari, A., Basili, R., Galadini, F., 2008. Sources of Mw 5+ earthquakes in northeastern Italy and western Slovenia: An updated view based on geological and seismological evidence. Tectonophysics 453, 157–176. doi:10.1016/j.tecto.2007.07.009.

Bus, Z., Grenerczy, G., Tóth, L., Mónus, P., 2009. Active crustal deformation in two seismogenic zones of the Pannonian region—GPS versus seismological observations. Tectonophysics 474, 343–352.

Caporali, A., Neubauer, F., Ostini, L., Stangl, G., Zuliani, D., 2013. Modeling surface GPS velocities in the Southern and Eastern Alps by finite dislocations at crustal depths. Tectonophysics 590, 136–150. doi:10.1016/j.tecto.2013.01.016.

Castellarin A., Cantelli L., Fesce A.M., Mercier J.L., Picotti V., Pini G.A., Prosser G., Selli L.,(1992). Alpine compressional tectonics in the Southern Alps. Relationships with the N-Apennines. Annales Tectonicae, 6, 62-94.

Castellarin, A., Cantelli, L., 2000. Neo-Alpine evolution of the Southern Eastern Alps. Journal of Geodynamics 30, 251–274. doi:10.1016/s0264-3707(99)00036-8.

Castellarin, A., Vai, G.B., Cantelli, L., 2006. The Alpine evolution of the Southern Alps around the Giudicarie faults: A Late Cretaceous to Early Eocene transfer zone. Tectonophysics 414, 203–223. doi:10.1016/j.tecto.2005.10.019.

Cheloni, D., D'Agostino, N. and Selvaggi, G., 2014. Interseismic coupling, seismic potential, and earthquake recurrence on the southern front of the Eastern Alps (NE Italy). Journal of Geophysical Research: Solid Earth. doi:10.1002/(ISSN)2169-9356.

Cheloni, D., D'Agostino, N., D'Anastasio, E., Selvaggi, G., 2012. Reassessment of the source of the 1976 Friuli, NE Italy, earthquake sequence from the joint inversion of high-precision levelling and triangulation data. Geophysical Journal International 190, 1279–1294. doi:10.1111/j.1365-246X.2012.05561.x.

Chiarabba, C., Jovane, L., Di Stefano, R., 2005. A new view to the Italian seismicity using 20 years of instrumental recordings. Tectonophysics 395, 251–268, doi:10.1016/j.tecto.2004.09.013.

D'Agostino, N., Avallone, A., Cheloni, D., D'Anastasio, E., Mantenuto, S., Selvaggi, G., 2008. Active tectonics of the Adriatic region from GPS and earthquake slip vectors. J Geophys Res 113. doi:10.1029/2008JB005860.

D'Agostino, N., Cheloni, D., Mantenuto, S., Selvaggi, G., Michelini, A., Zuliani, D., 2005. Strain accumulation in the southern Alps (NE Italy) and deformation at the northeastern boundary of Adria observed by CGPS measurements. Geophys. Res. Lett. 32, L19306. doi:10.1029/2005GL024266.

Danesi, S., Pondrelli, S., Salimbeni, S., Cavaliere, A., Serpelloni, E., Danecek, P., Lovati, S., Massa, M., 2015. Active deformation and seismicity in the Southern Alps (Italy): The Montello hill as a case study. Tectonophysics 653, 95–108. doi:10.1016/j.tecto.2015.03.028.

Decker K. and Peresson H., 1996. Tertiary kinematics in the Alpine- Carpathian-Pannonian system: links between thrusting, trans-formfaultingandcrustalextension.In:WesselyG,LieblW eds) Oil and gas in alpidic thrustbelts and basins of central and eastern Europe, EAGE Spec. Publ. 5, pp 69, 77.

Devoti, R., Zuliani, D., Braitenberg, C., Fabris, P., Grillo, B., 2015. Hydrologically induced slope deformations detected by GPS and clinometric surveys in the Cansiglio Plateau, southern Alps. Earth and Planetary Science Letters 419, 134–142. doi:10.1016/j.epsl.2015.03.023.

Doglioni, C., 1987. Tectonics of the Dolomites (Southern Alps, Northern Italy). Journal of Structural Geology 9, 181–193.

Doglioni, C., 1992. The Venetian Alps thrust belt, in: Thrust Tectonics. Springer Netherlands, Dordrecht, pp. 319–324. doi:10.1007/978-94-011-3066-0_29.

Dziewonski, A. M., T.-A. Chou and J. Woodhouse (1981). Determination of earthquake source parameters from waveform data for studies of global and regional seismicity, J. Geophys. Res. 86, 2825–2852.

Ekström, G. Dziewonski, A. M., Maternosvskaya, N. N. and Nettles, M. (2005). Global seismicity of 2003: Centroid-moment tensor solutions for 1087 earthquakes, Phys. Earth Planet. Inter., 148, 327-351.

Fantoni, R., Barbieri, C., Catellani, D., Castellarin, D., Di Giulio, A., Pessina, C., 2001. The re- cord of south-Alpine events in the Venetian foreland and foredeep. Geol. Paläont. Mitt. Innsbruck 25, 79–81.

Fejes, I., 2006. CONSORTIUM FOR CENTRAL EUROPEAN GPS GEODYNAMIC REFERENCE NETWORK (CEGRN CONSORTIUM), in: Pinter, N., Gyula, G., Weber, J., Stein, S., Medak, D. (Eds.), The Adria Microplate: GPS Geodesy, Tectonics and Hazards, Nato Science Series: IV: Earth and Environmental Sciences. Springer Netherlands, Dordrecht, pp. 183–193. doi:10.1007/1-4020-4235-3_12.

Floyd, M.A., Billiris, H., Paradissis, D., Veis, G., Avallone, A., Briole, P., McClusky, S., Nocquet, J.M., Palamartchouk, K., Parsons, B., England, P.C., 2010. A new velocity field for Greece: Implications for the kinematics and dynamics of the Aegean. J Geophys Res 115. doi:10.1029/2009JB007040.

Frisch, W., Kuhlemann, J., Dunkl, I., Brügel, A., 1998. Palinspastic reconstruction and topographic evolution of the Eastern Alps during late Tertiary tectonic extrusion. Tectonophysics 297, 1–15.

Frohlich, C., 1992. Triangle diagrams: ternary graphs to display similarity and diversity of earthquake focal mechanisms. Physics of the Earth and Planetary Interior, 75, 193–198.

Galadini, F., Galli, P., Molin, D. & Ciurletti G., 2001. Searching for the seismogenic source of the 1117 earthquake in northern Italy: a multidis- ciplinary approach, in The Use of Historical Data in Natural Hazards Assessment, pp. 3–27, eds Glade, T., Albini, P. & Frances, F., Kluwer Academic publishers, Dordrecht, the Netherlands.

Galadini, F., Poli, M.E., Zanferrari, A., 2005. Seismogenic sources potentially responsible for earthquakes with M≥ 6 in the eastern Southern Alps (Thiene-Udine sector, NE Italy). Geophysical Journal International 161, 739–762. doi:10.1111/j.1365-246X.2005.02571.x.

Gasperini, P., Lolli, B. and Vannucci, G., 2013b. Body wave magnitude mb is a good proxy of moment magnitude Mw for small earthquakes (mb<4.5-5.0), Seism. Res. Lett., 84, 6, 932-937, doi: 10.1785/0220130105.

Gasperini, P., Lolli, B., and Vannucci, G., 2013a. Empirical Calibration of Local Magnitude Data Sets Versus Moment Magnitude in Italy, Bull. Seism. Soc. Am. 103, 4, 2227-2246, doi: 10.1785/0120120356.

Gasperini, P., Lolli, B., Vannucci, G. and Boschi, E., 2012. Calibration of moment magnitude estimates for the European-Mediterranean and Italian regions, Geophysical Journal International 190, 1733-1745, doi: 10.1111/j.1365-246X.2012.05575.x.

Geuzaine, C. and Remacle, J.-F., 2009. Gmsh: a three-dimensional finite element mesh generator with built-in pre- and post-processing facilities. International Journal for Numerical Methods in Engineering 79(11), pp. 1309-1331.

Giardini, D., J. Woessner, L. Danciu, H. Crowley, F. Cotton, G. Grünthal, R. Pinho and G. Valensise and the SHARE consortium, 2014. SHARE European Seismic Hazard Map for Peak Ground Acceleration, 10% Exceedance Probabilities in 50 years, doi: 10.2777/30345, ISBN-13, 978-92-79-25148-1.

Grenerczy, G., Sella, G., Stein, S., Kenyeres, A., 2005. Tectonic implications of the GPS velocity field in the northern Adriatic region. Geophys. Res. Lett. 32.

Guidoboni, E., Comastri, A., Boschi, E., 2005. The “exceptional” earthquake of 3 January 1117 in the Verona area (northern Italy): A critical time review and detection of two lost earthquakes (lower Germany and Tuscany). J Geophys Res 110. doi:10.1029/2005JB003683.

Herak, D., Herak, M., Tomljenović, B., 2009. Seismicity and earthquake focal mechanisms in North-Western Croatia. Tectonophysics 465, 212–220. doi:10.1016/j.tecto.2008.12.005.

International Seismological Centre (2014). On-line ISC Bulletin, http://www.isc.ac.uk, Internat. Seis. Cent., Thatcham, United Kingdom.

Jackson, J. & Mckenzie, D., 1988. The relationship between plate motions and seismic moment tensors, and the rates of active deformation in the Mediterranean and Middle East, Geophys. J. Int., 93, 45–73.

Kanamori H. and D. L. Anderson, 1975. Theoretical basis of some empirical relations in seismology, Bull. Seism. Soc. Am., 65(5), 1073–1095.

Kastelic, V., Carafa, M.M.C., 2012. Fault slip rates for the active External Dinarides thrust-and-fold belt. Tectonics 31. doi:10.1029/2011TC003022.

Kastelic, V., Vannoli, P., Burrato, P., Fracassi, U., Tiberti, M.M., Valensise, G., 2013. Seismogenic sources in the Adriatic Domain. Marine and Petroleum Geology 42, 191–213. doi:10.1016/j.marpetgeo.2012.08.002.

Kostrov, V.V., 1974, Seismic moment and energy of earthquakes, and seismic flow of rock, Phys. Solid Earth, 1, 23–44.

Kostrov,V.V., 1974. Seismic moment and energy of earthquakes and seismic flow of rocks, Izv. Acad. Sci. USSR, Phys. Solid Earth, 1, 23–40.

Kreemer, C., G. Blewitt, E.C. Klein, 2014, A geodetic plate motion and Global Strain Rate Model, Geochemistry, Geophysics, Geosystems, 15, 3849-3889, doi:10.1002/2014GC005407.

Laubscher, H.P., 1996. Shallow and deep rotation in the Miocene Alps. Tectonics 15 (5), 1022-035.

Lolli B., Gasperini P., Mele F. M. and G. Vannucci, 2015. Recalibration of the distance correction term for local magnitude (ML) computations in Italy. Seismol. Res. Lett., 86, 5, doi: 10.1785/0220150020.

Lolli B., P. Gasperini and G. Vannucci, 2014. Empirical conversion between teleseismic magnitudes (mb and Ms) and moment magnitude (Mw) at the Global, Euro-Mediterranean and Italian scale, Geophys. J. Int., Vol. 199, 805–828, 2014, doi: 10.1093/gji/ggu264.

Loveless, J.P., Meade, B.J., 2011. Spatial correlation of interseismic coupling and coseismic rupture extent of the 2011 M W= 9.0 Tohoku-oki earthquake. Geophys. Res. Lett. 38. doi:10.1029/2011GL048561.

Loveless, J.P., Meade, B.J., 2016. Two decades of spatiotemporal variations in subduction zone coupling offshore Japan. Earth and Planetary Science Letters 436, 19–30. doi:10.1016/j.epsl.2015.12.033.

Maerten, F., 2005. Inverting for Slip on Three-Dimensional Fault Surfaces Using Angular Dislocations. Bulletin of the Seismological Society of America 95, 1654–1665. doi:10.1785/0120030181.

Massironi, M., Zampieri, D., Caporali, A., 2006. Miocene to Present major fault linkages through the Adriatic indenter and the Austroalpine–Penninic collisional wedge (Alps of NE Italy). In: Moratti, G., Chalouan, A. (Eds.), Active Tectonics of the Western Mediterranean Region and North Africa. In: Special Publications, vol. 262. Geological Society, London, pp. 245–258.

McCaffrey, R. 2002. Crustal block rotations and plate coupling, in Plate Boundary Zones, edited by S. Stein and J. T. Freymueller, pp. 101–122, AGU, Washington, D. C., doi:10.1029/GD030p0101.

Meade, B.J., Loveless, J.P., 2009. Block Modeling with Connected Fault-Network Geometries and a Linear Elastic Coupling Estimator in Spherical Coordinates. Bulletin of the Seismological Society of America 99, 3124–3139. doi:10.1785/0120090088.

Métois, M., D'Agostino, N., Avallone, A., Chamot-Rooke, N., Rabaute, A., Duni, L., Kuka, N., Koci, R., Georgiev, I., 2015. Insights on continental collisional processes from GPS data: Dynamics of the peri- Adriatic belts. J Geophys Res-Sol Ea n/a–n/a. doi:10.1002/2015JB012023.

Mitterschiffthaler, P. and Stangl, G., 2015. OLG REPRO2 - Start of reprocessing the densification networks, Vermessung & Geoinformation, 169-173.

Molinari, I., Morelli, A., 2011. EPcrust: a reference crustal model for the European Plate. Geophysical Journal International 185, 352–364. doi:10.1111/j.1365-246X.2011.04940.x.

Nocquet, J.M., Calais, E., 2003. Crustal velocity field of western Europe from permanent GPS array solutions, 1996–2001. Geophysical Journal International 154, 72–88.

Okada, Y., 1985. Surface deformation due to shear and tensile faults in a half-space, *Bull. Seism. Soc. Am.*, 75, 1435-1154.

Placer L. and Car J., 1998. Structure of Mt. Blegoš between the Inner and Outer Dinarides. Geologija, 40: 305-323.

Placer, L., 1999. Structural meaning of the Sava folds. Geologija 41, 191–221.

Poli, M.E., Peruzza, L., Rebez, A., Renner, G., Slejko, D., Zanferrari, A., 2002. New seismotectonic evidence from analysis of the 1976–1977 and 1977–1999 seismicity in Friuli (NE Italy). Boll. Geof. Teor. Appl. 43 (1–2), 53–78.

Poli, M.E., Renner, G., 2004. Normal focal mechanisms in the Julian Alps and Prealps: seismotectonic implications for the Italian-Slovenian border region. Boll Geof Teor Appl.

Pondrelli, S., Ekström, G., Morelli, A., 2001. Seismotectonic re-evaluation of the 1976 Friuli, Italy, seismic sequence. J. Seismol., 5, 73–83.

Pondrelli, S., Morelli, A. & Boschi, E., 1995. Seismic deformation in the Mediterranean area estimated by moment tensor summation, *Geophys. J. Int.,* 122, 938–952.

Pondrelli, S., S. Salimbeni, A. Morelli, G. Ekström, L. Postpischl, G. Vannucci, and E. Boschi (2011). European-Mediterranean Regional Centroid Moment Tensor Catalog: solutions for 2005-2008, Phys. Earth Planet. Int. 185, 74-81, doi: 10.1016/j.pepi.2011.01.007.

Ratschbacher, L., Frisch, W., Linzer, H.G., Merle, O., 1991b. Lateral extrusion in the Eastern Alps, part 2: structural analysis. Tectonics 10, 257–271.

Ratschbacher, L., Merle, O., Davy, P., Cobbold, P., 1991a. Lateral extrusion in the eastern Alps, Part 1: Boundary conditions and experiments scaled for gravity. Tectonics 10, 245–256. doi:10.1029/90TC02622.

Rovida, A., Camassi, R., Gasperini, P. and M. Stucchi (eds.) 2011. CPTI11, the 2011 version of the Parametric Catalogue of Italian Earthquakes. Milano, Bologna, http://emidius.mi.ingv.it/CPTI, Doi: 10.6092/INGV.IT-CPTI11.

Savage, J., 1983. A Dislocation Model of Strain Accumulation and Release at a Subduction Zone. J Geophys Res 88, 4984–4996.

Schmid, S.M., F genschuh, B., Kissling, E., Schuster, R., 2004. Tectonic map and overall architecture of the Alpine orogen. Eclogae geol. Helv. 97, 93–117. doi:10.1007/s00015-004-1113-x.

Scognamiglio, L., E. Tinti, and A. Michelini (2009). Real-Time Determination of Seismic Moment Tensor for the Italian Region, Bull. Seism. Soc. Am. 99, 4, 2223-2242, doi: 10.1785/0120080104.

Serpelloni, E., Anzidei, M., Baldi, P., Casula, G., Galvani, A., 2005. Crustal velocity and strain-rate fields in Italy and surrounding regions: new results from the analysis of permanent and non-permanent GPS networks. Geophysical Journal International 161, 861–880. doi:10.1111/j.1365-246X.2005.02618.x.

Serpelloni, E., Casula, G., Galvani, A., Anzidei, M., Baldi, P., 2006. Data analysis of permanent GPS networks in Italy and surrounding regions: application of a distributed processing approach. Ann Geophys-Italy 49, 897–928.

Serpelloni, E., Cavaliere, A., 2010. A Complementary GPS Survey Mode for Precise Crustal Deformation Monitoring: The Conegliano–Montello Active Thrust Semicontinuous GPS, Network. (RT131, http://portale.ingv.it/produzione-scientifica/rapporti-tecnici-ingv/copy_of_numeri-pubblicati-2010).

Serpelloni, E., Faccenna, C., Spada, G., Dong, D., Williams, S.D.P., 2013. Vertical GPS ground motion rates in the Euro- Mediterranean region: New evidence of velocity gradients at different spatial scales along the Nubia- Eurasia plate boundary. J Geophys Res-Sol Ea 118, 6003–6024. doi:10.1002/2013JB010102.

Serpelloni, E., Vannucci, G., Pondrelli, S., Argnani, A., Casula, G., Anzidei, M., Baldi, P., Gasperini, P., 2007. Kinematics of the Western Africa–Eurasia plate boundary from focal mechanisms and GPS data. Geophys. J. Int. 169, 1180–1200, doi:10.1111/j.1365-246X.2007.03367.x.

Sipkin, S. A. (1982). Estimation of earthquake source parameters by the inversion of wave-form data: synthetic waveforms, Phys. Earth Planet. Int. 30, 242–259.

Sipkin, S. A. (1994). Rapid determination of global moment-tensor solutions, Geophys. Res. Lett. 21 no. 16, 1667–1670.

Smith, W. H. F., and P. Wessel, 1990, Gridding with a Continuous Curvature Surface in Tension, Geophysics, 55, 293-305.

Stein, S., Gordon, R.G., 1984. Statistical tests of additional plate boundaries from plate motion inversions. Earth and Planetary Science Letters 69, 401–412.

Stucchi, M., Rovida, A., Gomez Capera, A.A., Alexandre, P., Camelbeeck, T., Demircioglu, M.B., Gasperini, P., Kouskouna, V., Musson, R.M.W., Radulian, M., Sesetyan, K., Vilanova, S., Baumont, D., Bungum, H., Fäh, D., Lenhardt, W., Makropoulos, K., Martinez Solares, J.M., Scotti, O., Živčić, M., Albini, P., Batlló, J., Papaioannou, C., Tatevossian, R., Locati, M., MELETTI, C., Viganò, D., Giardini, D., 2012. The SHARE European Earthquake Catalogue (SHEEC) 1000–1899. J Seismol 17, 523–544. doi:10.1007/s10950-012-9335-2.

Tape, C., Musé, P., Simons, M., Dong, D., Webb, F., 2009. Multiscale estimation of GPS velocity fields. Geophysical Journal International, 179, 945–971. doi:10.1111/j.1365-246X.2009.04337.x.

Thatcher W. 2003. GPS constraints on the kinematics of continental deformation. *Int. Geol. Rev.* 45:191–212.

Vannucci G., P. Imprescia, and P. Gasperini (2010). Deliverable n. 2 of the UR2.05 in the INGV-DPC S1 project (2007-2009). INGV-DPC Internal report and database.

Vannucci, G., and P. Gasperini (2003). A database of revised fault plane solutions for Italy and surrounding regions, Computers and Geosciences 29, 903-909.

Vannucci, G., and P. Gasperini (2004). The new release of the database of earthquake mechanisms of the Mediterranean area (EMMA Version 2), Annals of Geophysics 47, 307-334.

Vannucci, G., Pondrelli, S., Argnani, A., Morelli, A., Gasperini, P. & Boschi, E. (2004). An Atlas of Mediterranean seismicity, *Ann. Geophys.*, 47(Suppl 1), 247–306.

Viganò, A., Bressan, G., Ranalli, G., Martin, S., 2008. Focal mechanism inversion in the Giudicarie–Lessini seismotectonic region (Southern Alps, Italy): Insights on tectonic stress and strain. Tectonophysics 460, 106–115. doi:10.1016/j.tecto.2008.07.008.

Wessel, P., W. H. F. Smith, R. Scharroo, J. F. Luis, and F. Wobbe, Generic Mapping Tools: Improved version released, EOS Trans. AGU, 94, 409-410, 2013.

Westaway, R., 1992. Seismic moment summation for historical earthquakes in Italy: tectonic implications, J. Geophys. Res., 97, 15 437–15 464.

Figure Captions

Figure 1. Tectonic map of the study area, with the major tectonic lineaments shown in black. The seismicity since 1000 is extracted from the integrated catalogue discusses in Section 3. Major historical events (Mw>6) are shown as yellow stars. The green lines show national boundaries (regional boundaries only for Italy). AR: Arba-Ragona thrust; BF: Brenner fault; BG: Ballino Garda thrust; BL: Belluno thrust; BS: Mt. Baldo-Mt. Stivo thrust; BV: Bassano-Valdobbiadene thrust; CA: Cansiglio thrust; CF: Celje fault; CT: Cicarija thrust; DF: Donat fault; FL: Fadalto line; FS: Fella-Sava line; GB: Gorenjska basin; GK: Gemona-Kobarid thrust; IF: Idrja fault; IsF: Iseltal Fault; IL: Inntal line; PAF (IN): Periadriatic fault - Insubric line; ISAM: Innsbruck–Salzburg–Amstetten fault; JAT: Julian Alps thrust; KB: Klagenfurt basin; LL: Lavanttal line; LM: Lessini Mountains; MD: Medea thrust; MH: Möll Hochstuhl fault; MM: Mur-Mürz fault; MT: Montello thrust; PAF (NG): Periadriatic fault - North Giudicarie line; PAF (PG): Periadriatic fault - Pusteri-Gailtal line; PM: Polcenigo-Maniago thrust; PT: Pozzuolo thrust; RF: Raša fault; SA: Sarca faults; SB: Savinja basin; SEMP: Salzachtal-Ennstal-Mariazell-Puchberg line; SF: Sava fault; SG: South Giudicarie line; ST: Susans-Tricesimo thrust; SV: Schio-Vicenza line; TBC: Thiene-Bassano-Cornuda thrust; VB: Vienna basin; VS: Val-Sugana thrust; VT: Val Trompia thrust; ZF: Žužemberk fault.

Figure 2. Maps of the seismic flux (yearly seismic moment release rate x unit area) computed from the integrated seismic catalogue for different time-intervals (shown in upper-left corners). The maps show the interpolated and continuous seismic flux obtained from the raw data in the 0.1x0.1° cells shown in Figure S2. Epicenters of Mw≥6 historical earthquakes (stars), occurred in the time-interval of each sub-plot are also shown.

Figure 3. A) Map of the focal mechanisms (FMs) dataset (see also Figure S2a), compiled in this work. Only FMs confined in the upper crust (EPCrust model of Molinari and Morelli, 2011) are shown. B) Tectonic regimes obtained from the seismic summation of FMs in hexagonal area

with 10 km of side. Hexagonal areas are represented with an RGB color, following the plot of the corresponding FM sum (Figure S2b) in the Frohlich triangle diagram: blue indicates normal faulting, red thrust faulting and green strike-slip faulting, respectively. The black and white arrows in each hexagonal element show the P- and T-axes, plotted on the horizontal plane, respectively, of the corresponding FM sum (Fig. S2b). The dashed gray lines show the small circles around the geodetic pole of rotation describing the motion direction of Adria relative to Eurasia.

Figure 4. A) Horizontal GPS velocities (white arrows) in a fixed Eurasian reference frame, with 95% confidence error ellipses, superimposed on a map of the GPS speed obtained using the multiscale method described in Section 4.2. The dashed gray lines show the small circles around the geodetic pole of rotation (black star) showing the motion direction of Adria relative to Eurasia. B) Eurasia-fixed GPS velocities superimposed on a map of east component of the multiscale velocity field.

Figure 5. Strain-rate field obtained using the multiscale approach described in Section 4. The black diverging and converging arrows show the axes of the principal strain-rates, which are superimposed on a map of the total strain-rate field (i.e., the scalar value of the strain-rate tensor) defined as the square root of the sum of squares of all its components. The red and green arrows show the P- and T-axes, respectively, shown in Fig. 3. The dashed purple lines show the small circles around the geodetic pole of rotation describing the motion direction of Adria relative to Eurasia. The upper-left inset shows the scalar strain-rate map where the black dashed line contours the region with strain-rate values greater than 0.15x10-7yr-1 together with Mw>6 historical earthquakes, as in Fig. 1.

Figure 6. GPS velocities (dark gray arrows with 95% confidence error ellipses) given in different block-fixed reference frames. The yellow squares indicate GPS stations used to define the reference frames. The red symbols highlight kinematic features discussed in Section 4.3). A) velocities given with respect to the Adriatic microplate; B) velocities given with respect to a reference frame obtained by minimizing the velocities of GPS sites located in the Dolomitic Southern Alps; C) velocities given with respect to a reference frame obtained by minimizing the velocities of GPS sites located in the Pannonian basin area included in this work.

Figure 7. Block model geometry (black thick lines) with observed (blue arrows, with 95% error ellipses) and modeled (red arrows) velocities in the Eurasia-fixed reference frame. The light grey boxes show horizontal projection of rectangular dislocation planes of non-vertical faults. The light grey lines show faults and/or tectonic lineaments as in Fig. 1. The green lines show fault traces from the SHARE database. The model geometry shown corresponds to Model 2 of Fig. S9.

Figure 8. Model slip-rates. A) dip-slip and tensile rates, with red and blue showing inverse and extensional components, respectively. B) strike-slip components, with red and blue showing right-lateral and left-lateral rates components, respectively.

Figure 9. Results from the variable back-slip model inversion. A) Dip-slip components, with red and blue colors showing inverse and normal rates components, respectively; B) Strike-slip components, with red and blue colors showing right-lateral and left-lateral rates components, respectively; C) interseismic coupling, between 0 (fully uncoupled) and 1 (fully coupled); D) resolution length (RL) estimated following Ader et al. (2013).

Figure 10a. Cross sections showing observed and modeled velocities (profile parallel or profile normal components) across major fault systems of the ESA. The upper-left inset shows blocks from Fig. 7, observed GPS velocities (without error ellipses) and the cross sections (dashed black boxes) with the white starts indicating the starting point for each cross-section. In the cross sections, where "p" and "n" mean profile parallel and profile normal components, respectively, the red circles show the observed velocity components (with error bars showing 1σ uncertainties) of GPS stations included in the dashed boxes. The continuous grey thick line in each plot shows the modeled velocity components obtained from the heterogeneous slip model for the ESA thrust front (Fig. 9), with the dashed thick lines showing the modeled velocities from the uniform slip model (Fig. 7). The yellow area is the envelope of the minimum and maximum values of the modeled velocity components in the swath profiles. The dark grey areas show the average (median) topography in the profile swath, with the light grey and white areas showing the maximum and minimum elevations, respectively. The distribution of seismicity with depth (in km) along each cross-section is shown by the colored circles, where the grey and black lines indicating the depth of the UPC and the depth of the seismogenic layer (75% of seismicity), as discussed in Section 3. The dark grey dashed lines show the blocks-bounding faults (used in the uniform slip model) crossed by the profile.

Figure 10b. Continuation of Fig. 10a.

Figure 11. Comparison between seismic and geodetic flux along the ESA front in the Veneto-Friuli and Slovenia segments. The blue, grey and black lines show the seismic flux computed from 1005, 1600 and 1900, respectively. The continuous and dashed purple lines show the geodetic flux calculated from the geodetic strain-rate field assuming as the seismogenic depth the upper-crust and the 75% percentile layer (Figs S4 and S5), respectively. The red line shows the variation of the strain-rate values computed from the model velocity field. All lines show the maximum values of the estimated flux within the swath profiles A-B and C-D. The maximum, average and minimum swath topography is also shown in grey colors. The colored circles show the Mw>5.0 earthquakes occurred within the swath profiles from the merged seismic catalogue, plotted as a function of time and distance along the profile.

Figure 12. Schematic tectonic and kinematic map showing the major findings discussed in this work. The dashed red lines (with question marks) show discussed or less constrained blocks-bounding faults. The grey arrows show surface velocities, with respect to Eurasia, from the block model discussed in Section 5.3. The dashed gray lines show the small circles around the geodetic pole of rotation showing the motion direction of Adria relative to Eurasian plate estimated from the block model (Tab. S5).

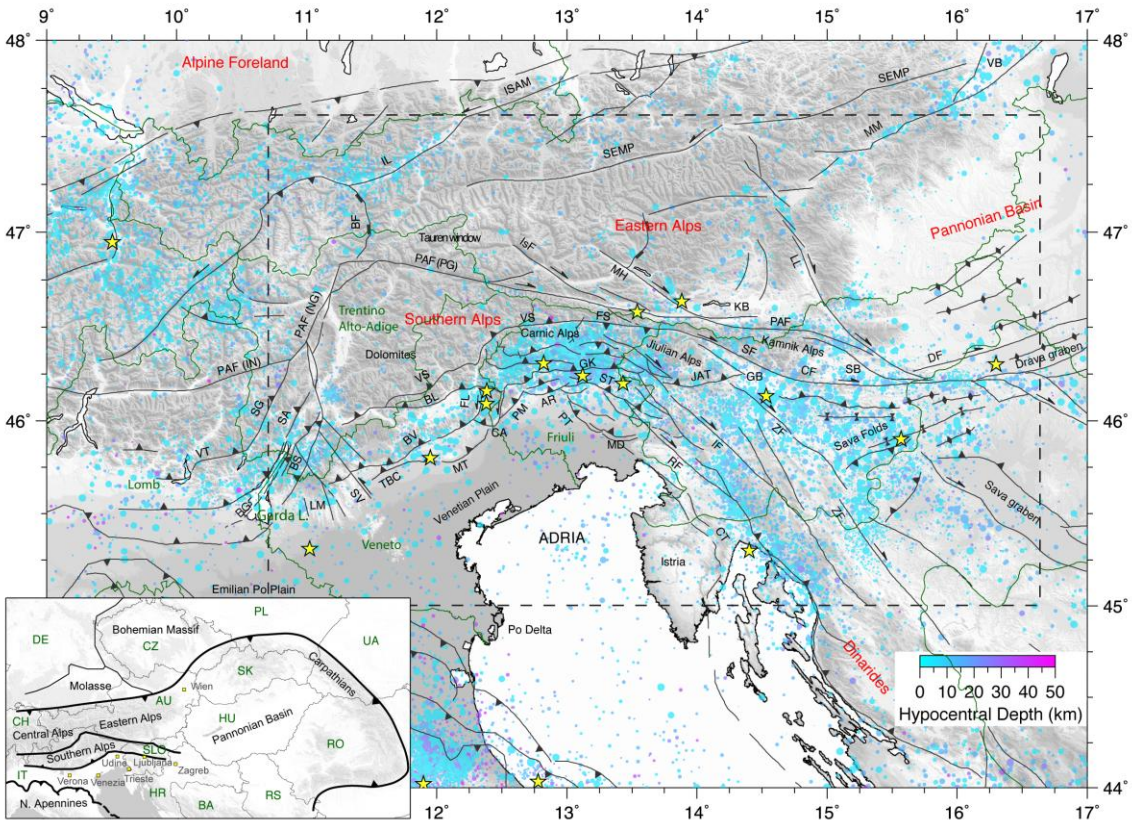

Figure 1. Tectonic map of the study area, with the major tectonic lineaments shown in black. The seismicity since 1000 is extracted from the integrated catalogue discusses in Section 3. Major historical events (Mw>6) are shown as yellow stars. The green lines show national boundaries (regional boundaries only for Italy). AR: Arba-Ragona thrust; BF: Brenner fault; BG: Ballino Garda thrust; BL: Belluno thrust; BS: Mt. Baldo-Mt. Stivo thrust; BV: Bassano-Valdobbiadene thrust; CA: Cansiglio thrust; CF: Celje fault; CT: Cicarija thrust; DF: Donat fault; FL: Fadalto line; FS: Fella-Sava line; GB: Gorenjska basin; GK: Gemona-Kobarid thrust; IF: Idrja fault; IsF: Iseltal Fault; IL: Inntal line; PAF (IN): Periadriatic fault - Insubric line; ISAM: Innsbruck–Salzburg–Amstetten fault; JAT: Julian Alps thrust; KB: Klagenfurt basin; LL: Lavanttal line; LM: Lessini Mountains; MD: Medea thrust; MH: Möll Hochstuhl fault; MM: Mur-Mürz fault; MT: Montello thrust; PAF (NG): Periadriatic fault - North Giudicarie line; PAF (PG): Periadriatic fault - Pusteri-Gailtal line; PM: Polcenigo-Maniago thrust; PT: Pozzuolo thrust; RF: Raša fault; SA: Sarca faults; SB: Savinja basin; SEMP: Salzachtal-Ennstal-Mariazell-Puchberg line; SF: Sava fault; SG: South Giudicarie line; ST: Susans-Tricesimo thrust; SV: Schio-Vicenza line; TBC: Thiene-Bassano-Cornuda thrust; VB: Vienna basin; VS: Val-Sugana thrust; VT: Val Trompia thrust; ZF: Žužemberk fault.

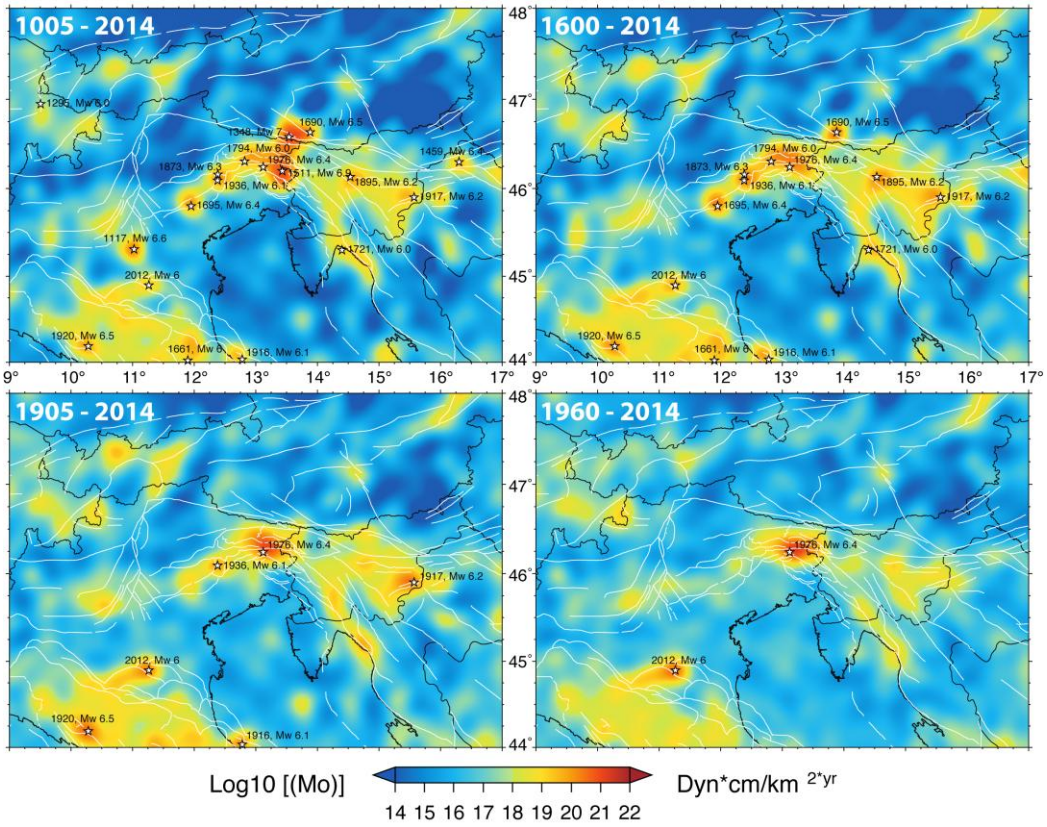

Figure 2. Maps of the seismic flux (yearly seismic moment release rate x unit area) computed from the integrated seismic catalogue for different time-intervals (shown in upper-left corners). The maps show the interpolated and continuous seismic flux obtained from the raw data in the 0.1x0.1° cells shown in Figure S2. Epicenters of Mw≥6 historical earthquakes (stars), occurred in the time-interval of each sub-plot are also shown.

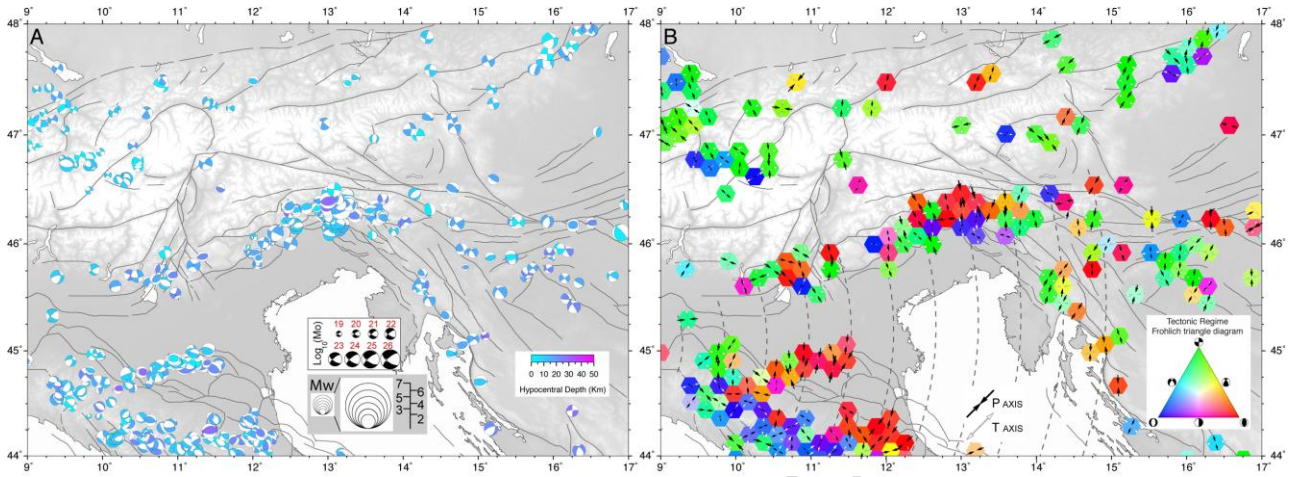

Figure 3. A) Map of the focal mechanisms (FMs) dataset (see also Figure S2a), compiled in this work. Only FMs confined in the upper crust (EPCrust model of Molinari and Morelli, 2011) are shown. B) Tectonic regimes obtained from the seismic summation of FMs in hexagonal area with 10 km of side. Hexagonal areas are represented with an RGB color, following the plot of the corresponding FM sum (Figure S2b) in the Frohlich triangle diagram: blue indicates normal faulting, red thrust faulting and green strike-slip faulting, respectively. The black and white arrows in each hexagonal element show the P- and T-axes, plotted on the horizontal plane, respectively, of the corresponding FM sum (Fig. S2b). The dashed gray lines show the small circles around the geodetic pole of rotation describing the motion direction of Adria relative to Eurasia.

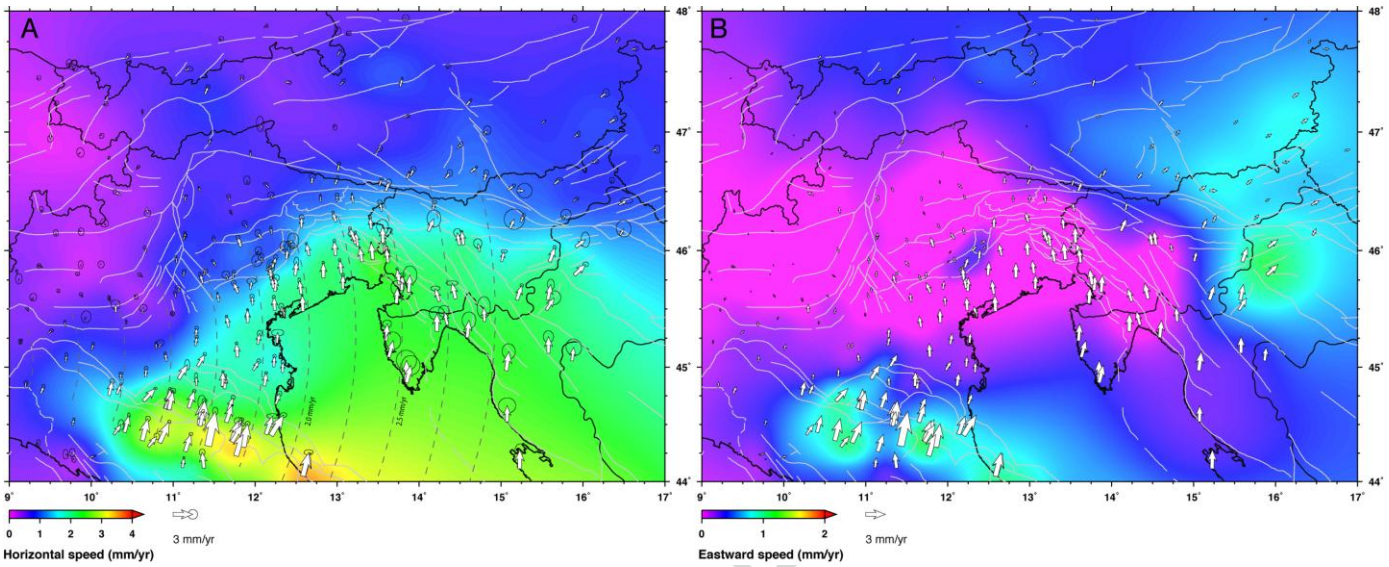

Figure 4. A) Horizontal GPS velocities (white arrows) in a fixed Eurasian reference frame, with 95% confidence error ellipses, superimposed on a map of the GPS speed obtained using the multiscale method described in Section 4.2. The dashed gray lines show the small circles around the geodetic pole of rotation (black star) showing the motion direction of Adria relative to Eurasia. B) Eurasia-fixed GPS velocities superimposed on a map of east component of the multiscale velocity field.

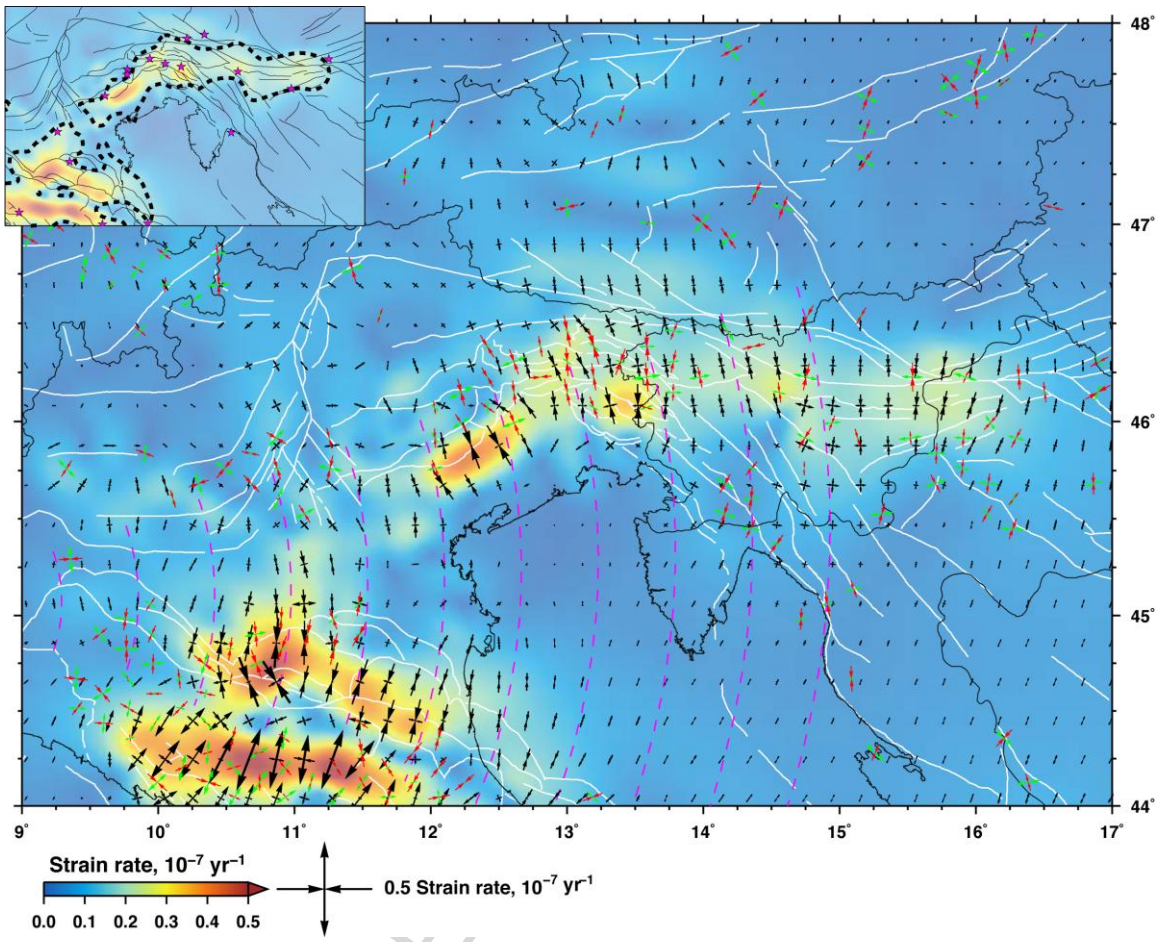

Figure 5. Strain-rate field obtained using the multiscale approach described in Section 4. The black diverging and converging arrows show the axes of the principal strain-rates, which are superimposed on a map of the total strain-rate field (i.e., the scalar value of the strain-rate tensor) defined as the square root of the sum of squares of all its components. The red and green arrows show the P- and T-axes, respectively, shown in Fig. 3. The dashed purple lines show the small circles around the geodetic pole of rotation describing the motion direction of Adria relative to Eurasia. The upper-left inset shows the scalar strain-rate map where the black dashed line contours the region with strain-rate values greater than 0.15x10-7yr-1 together with Mw>6 historical earthquakes, as in Fig. 1.

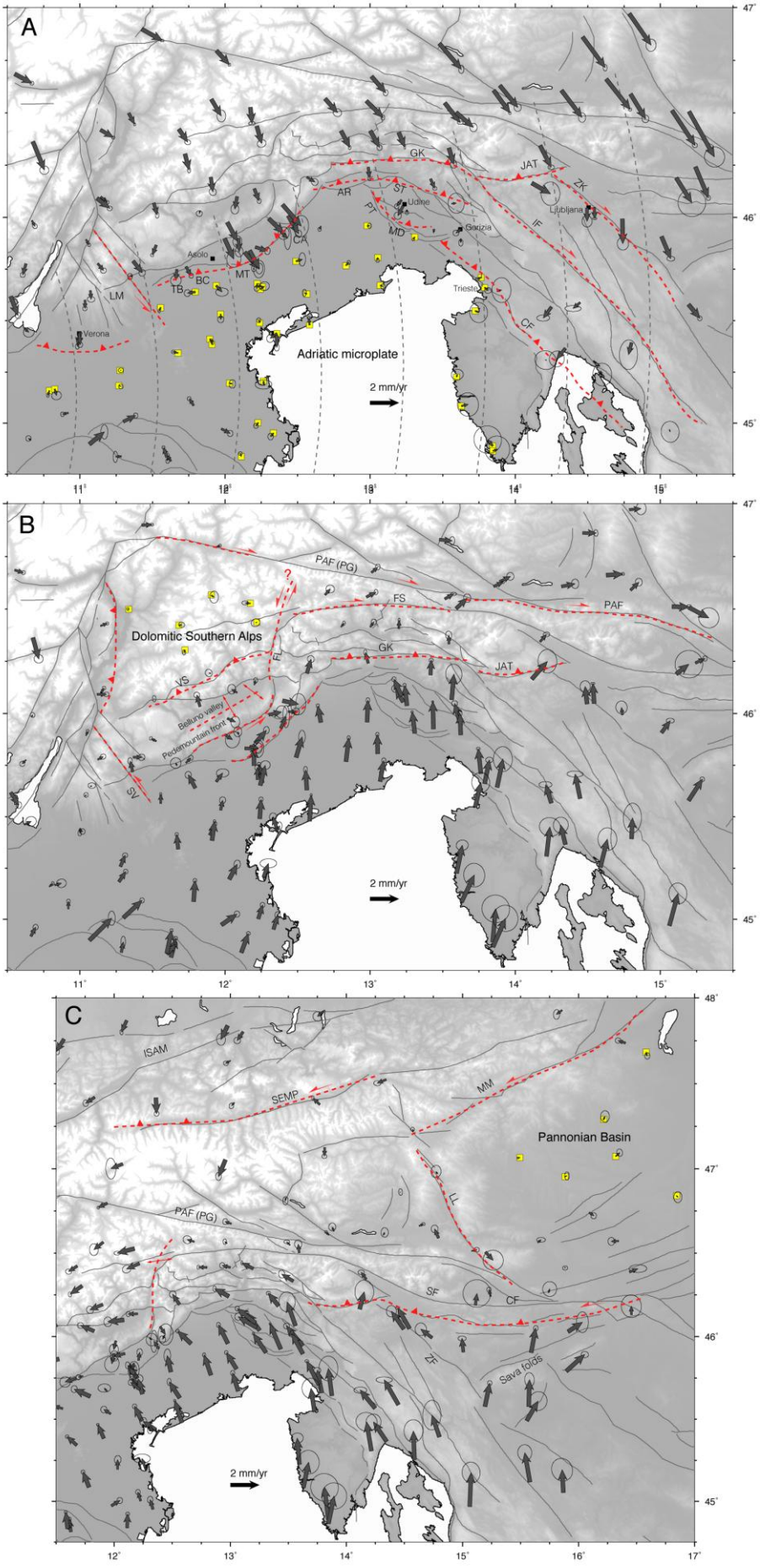

Figure 6. GPS velocities (dark gray arrows with 95% confidence error ellipses) given in different block-fixed reference frames. The yellow squares indicate GPS stations used to define the reference frames. The red symbols highlight kinematic features discussed in Section 4.3). A) velocities given with respect to the Adriatic microplate; B) velocities given with respect to a reference frame obtained by minimizing the velocities of GPS sites located in the Dolomitic Southern Alps; C) velocities given with respect to a reference frame obtained by minimizing the velocities of GPS sites located in the Pannonian basin area included in this work.

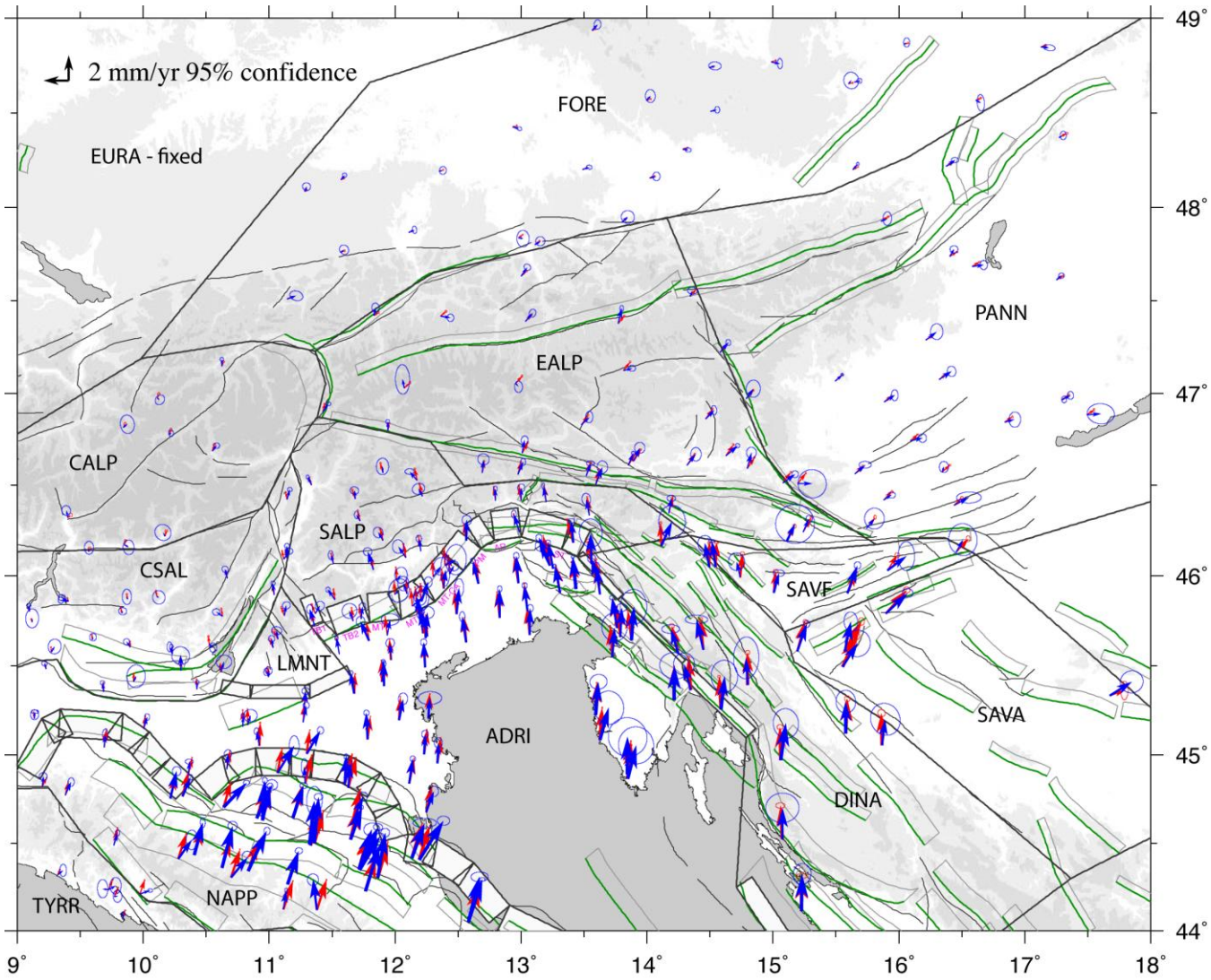

Figure 7. Block model geometry (black thick lines) with observed (blue arrows, with 95% error ellipses) and modeled (red arrows) velocities in the Eurasia-fixed reference frame. The light grey boxes show horizontal projection of rectangular dislocation planes of non-vertical faults. The light grey lines show faults and/or tectonic lineaments as in Fig. 1. The green lines show fault traces from the SHARE database. The model geometry shown corresponds to Model 2 of Fig. S9.

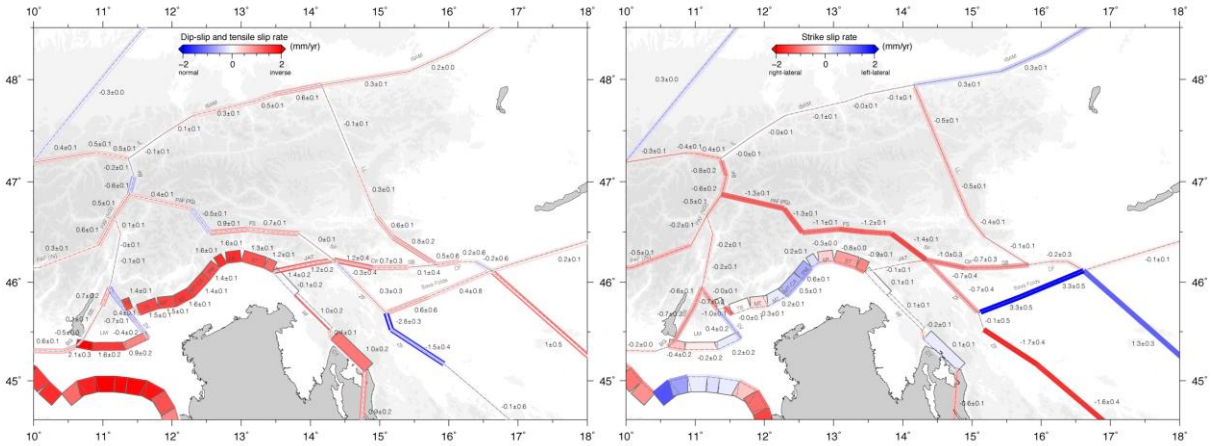

Figure 8. Model slip-rates. A) dip-slip and tensile rates, with red and blue showing inverse and extensional components, respectively. B) strike-slip components, with red and blue showing right-lateral and left-lateral rates components, respectively.

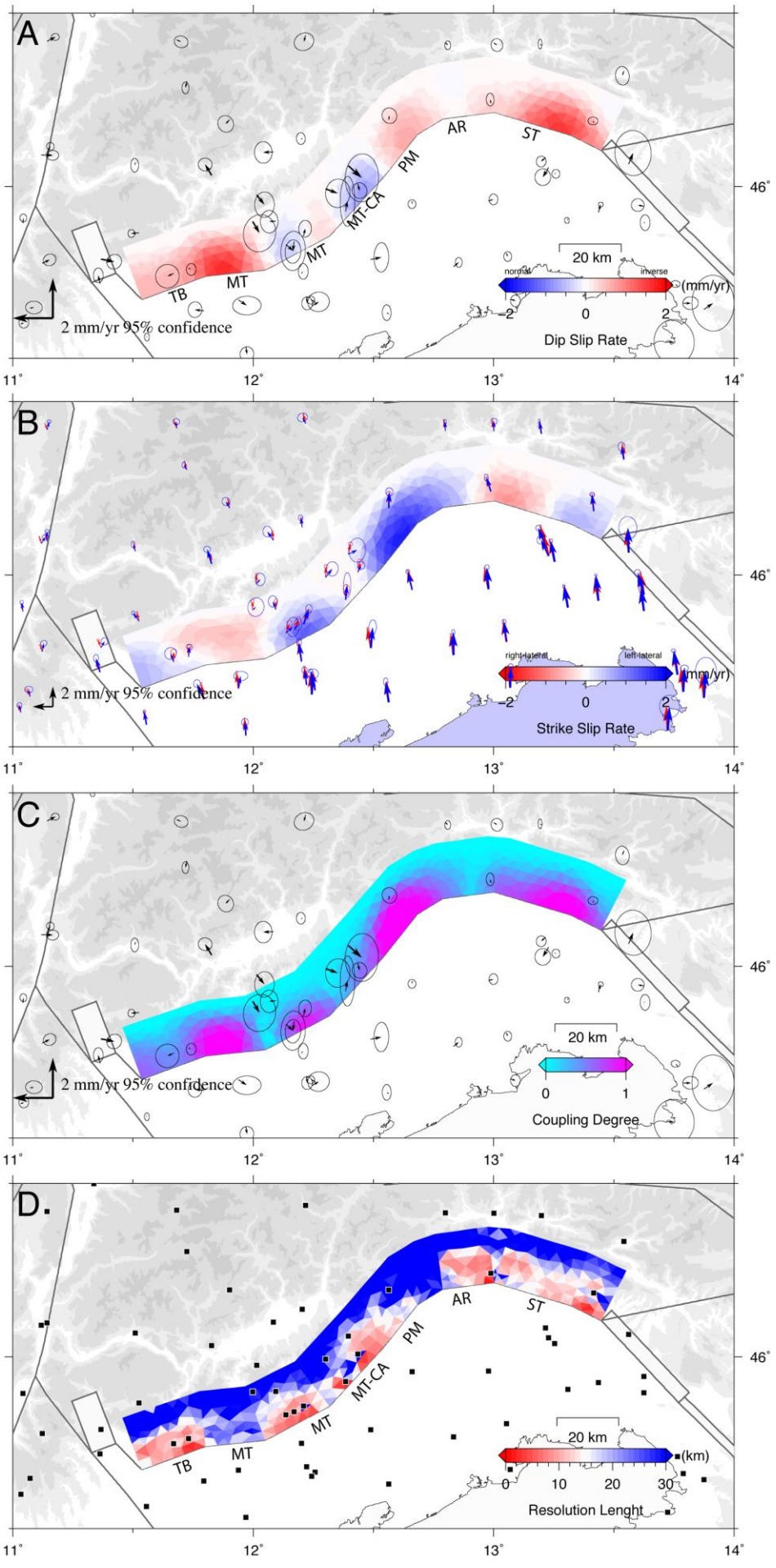

Figure 9. Results from the variable back-slip model inversion. A) Dip-slip components, with red and blue colors showing inverse and normal rates components, respectively; B) Strike-slip components, with red and blue colors showing right-lateral and left-lateral rates components, respectively; C) interseismic coupling, between 0 (fully uncoupled) and 1 (fully coupled); D) resolution length (RL) estimated following Ader et al. (2013).

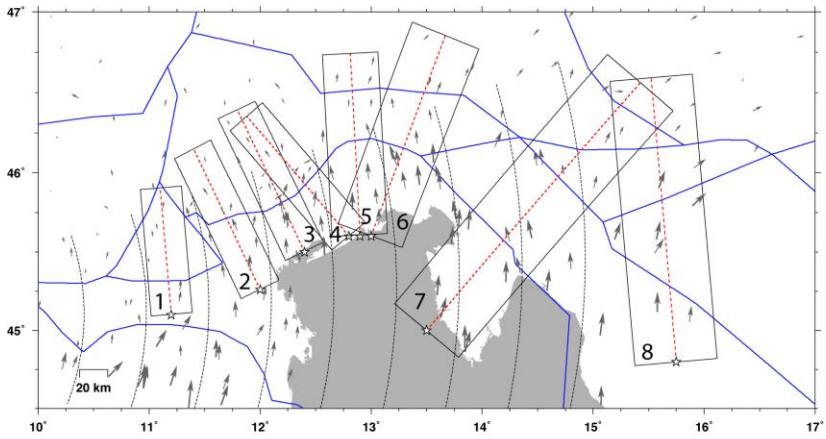
47°
46°
45°
10°
11°
12°
13°
14°
15°
16°
17°
20 km
1
2
3
4
5
6
7
8

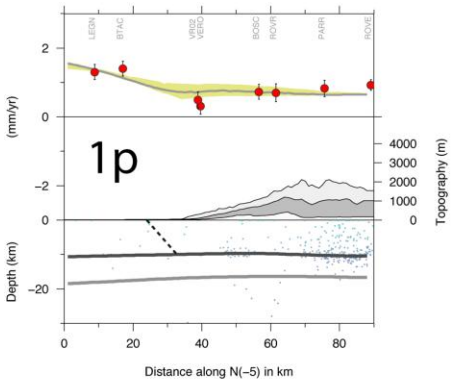
1p
(mm/yr)
Depth (km)
Topography (m)
Distance along N(−5) in km

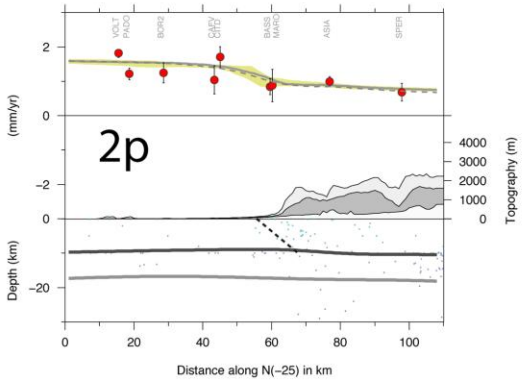
2p
(mm/yr)
Depth (km)
Topography (m)
Distance along N(−25) in km

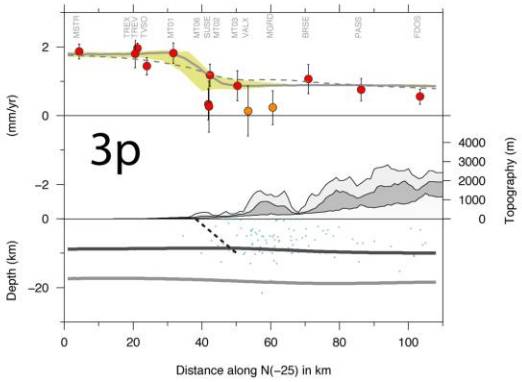
3p
(mm/yr)
Depth (km)
Topography (m)
Distance along N(−25) in km

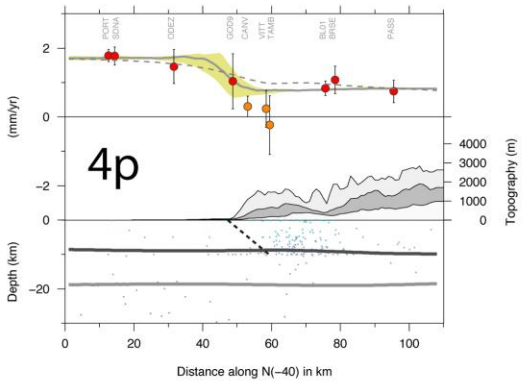
4p
(mm/yr)
Depth (km)
Topography (m)
Distance along N(−40) in km

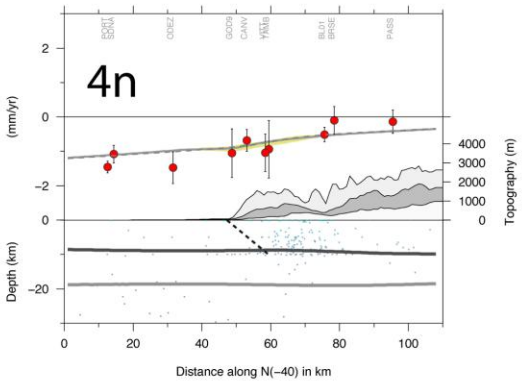
4n
(mm/yr)
Depth (km)
Topography (m)
Distance along N(−40) in km

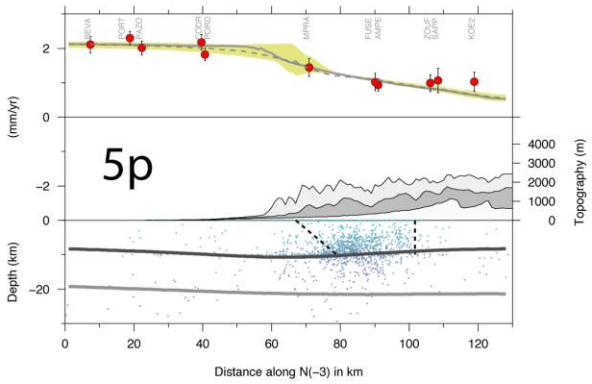
5p
(mm/yr)
Depth (km)
Topography (m)
Distance along N(−3) in km

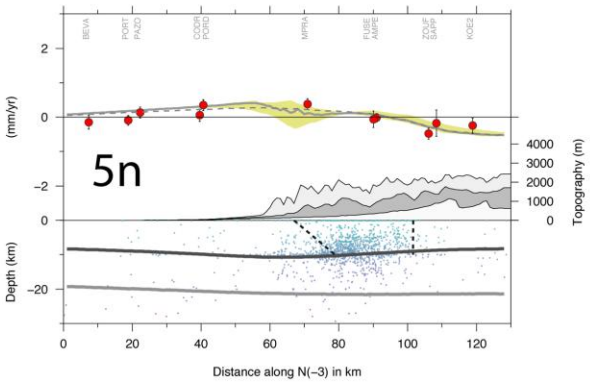
5n
(mm/yr)
Depth (km)
Topography (m)
Distance along N(−3) in km

Figure 10a. Cross sections showing observed and modeled velocities (profile parallel or profile normal components) across major fault systems of the ESA. The upper-left inset shows blocks from Fig. 7, observed GPS velocities (without error ellipses) and the cross sections (dashed black boxes) with the white starts indicating the starting point for each cross-section. In the cross sections, where "p" and "n" mean profile parallel and profile normal components, respectively, the red circles show the observed velocity components (with error bars showing 1σ uncertainties) of GPS stations included in the dashed boxes. The continuous grey thick line in each plot shows the modeled velocity components obtained from the heterogeneous slip model for the ESA thrust front (Fig. 9), with the dashed thick lines showing the modeled velocities from the uniform slip model (Fig. 7). The yellow area is the envelope of the minimum and maximum values of the modeled velocity components in the swath profiles. The dark grey areas show the average (median) topography in the profile swath, with the light grey and white areas showing the maximum and minimum elevations, respectively. The distribution of seismicity with depth (in km) along each cross-section is shown by the colored circles, where the grey and black lines indicating the depth of the UPC and the depth of the seismogenic layer (75% of seismicity), as discussed in Section 3. The dark grey dashed lines show the blocks-bounding faults (used in the uniform slip model) crossed by the profile.

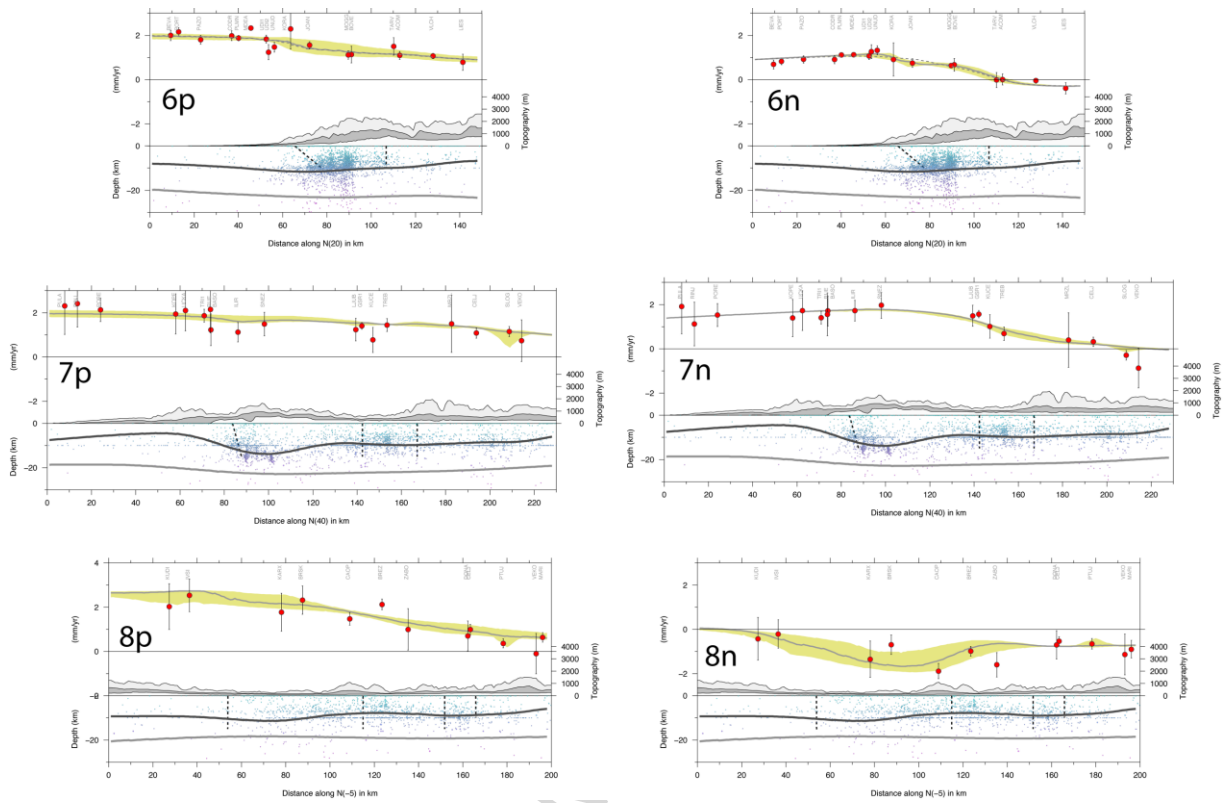

Figure 10b. Continuation of Fig. 10a.

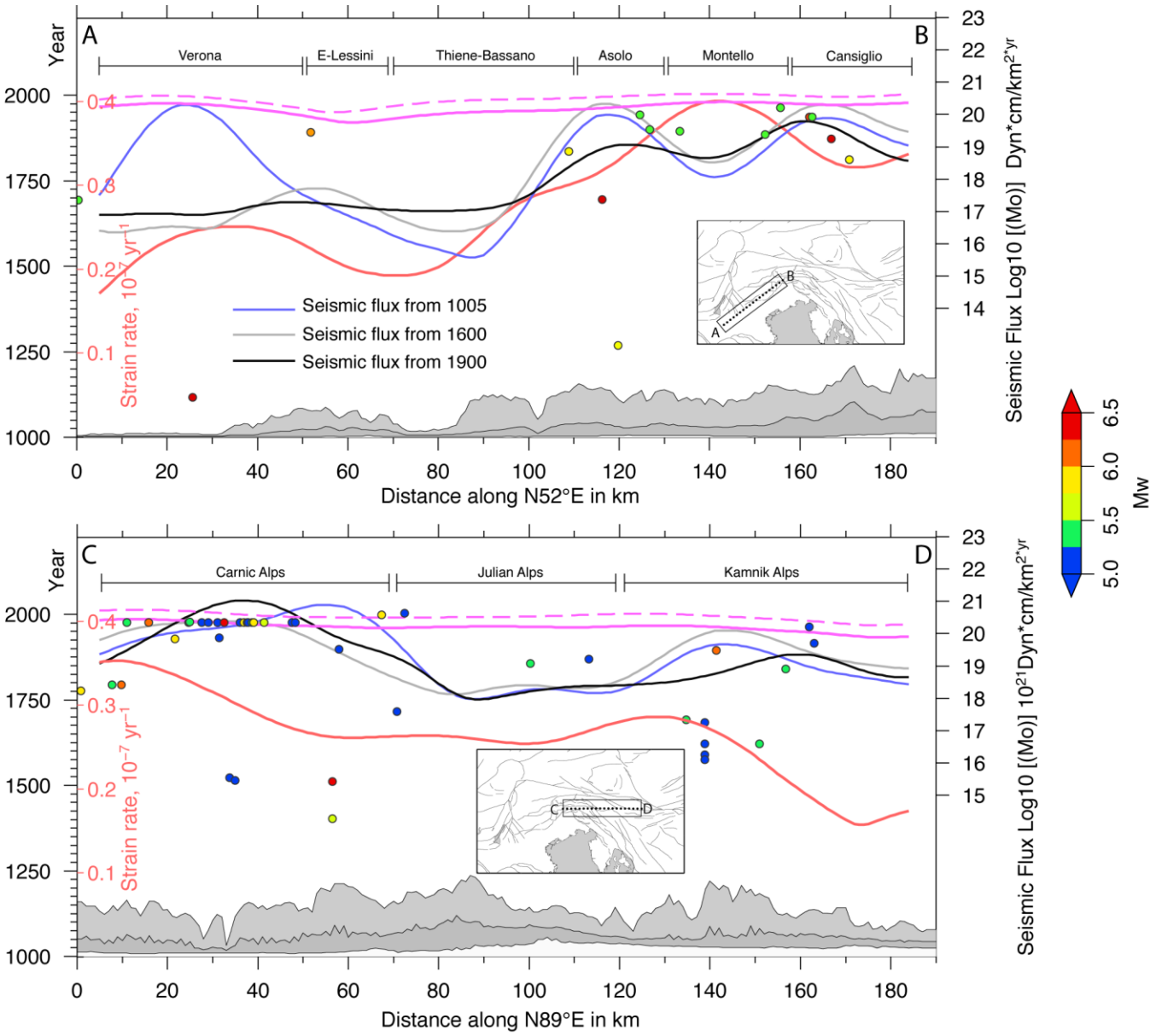

Figure 11. Comparison between seismic and geodetic flux along the ESA front in the Veneto-Friuli and Slovenia segments. The blue, grey and black lines show the seismic flux computed from 1005, 1600 and 1900, respectively. The continuous and dashed purple lines show the geodetic flux calculated from the geodetic strain-rate field assuming as the seismogenic depth the upper-crust and the 75% percentile layer (Figs S4 and S5), respectively. The red line shows the variation of the strain-rate values computed from the model velocity field. All lines show the maximum values of the estimated flux within the swath profiles A-B and C-D. The maximum, average and minimum swath topography is also shown in grey colors. The colored circles show the Mw>5.0 earthquakes occurred within the swath profiles from the merged seismic catalogue, plotted as a function of time and distance along the profile.

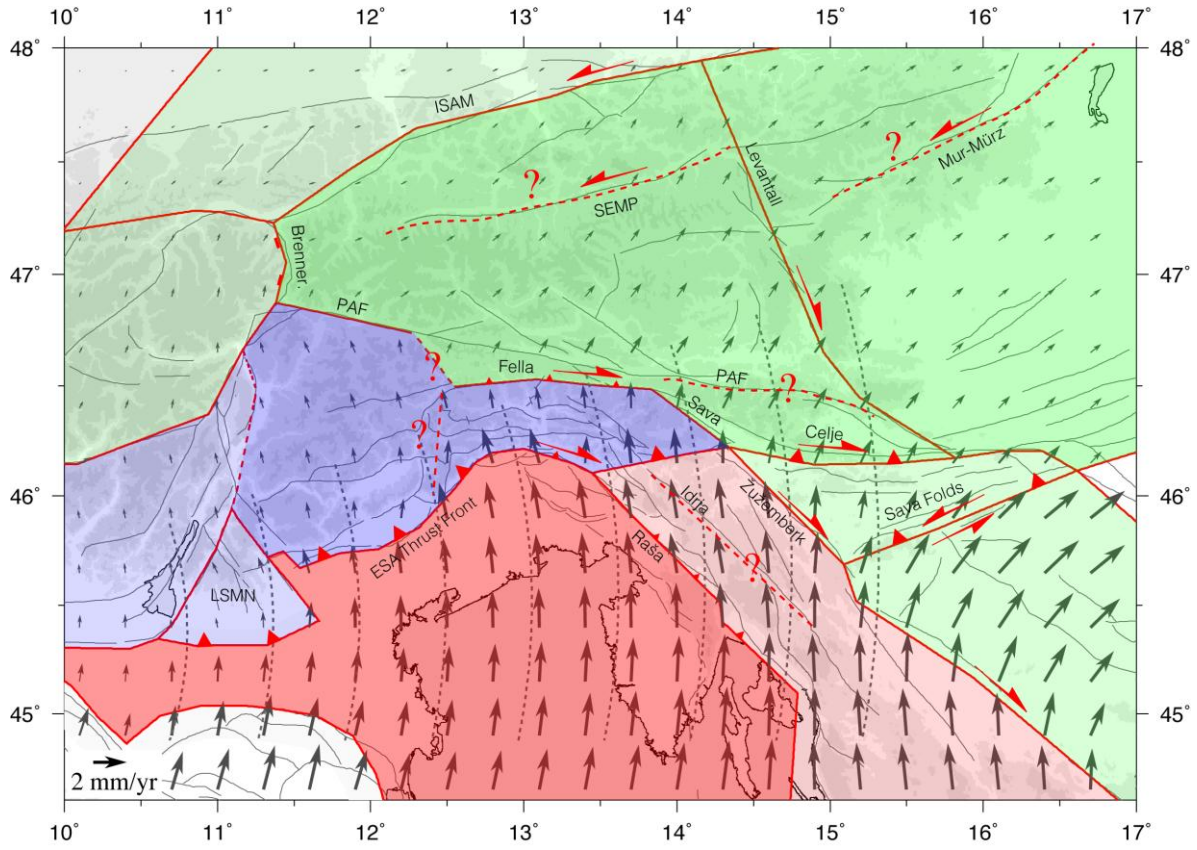

Figure 12. Schematic tectonic and kinematic map showing the major findings discussed in this work. The dashed red lines (with question marks) show discussed or less constrained blocks-bounding faults. The grey arrows show surface velocities, with respect to Eurasia, from the block model discussed in Section 5.3. The dashed gray lines show the small circles around the geodetic pole of rotation showing the motion direction of Adria relative to Eurasian plate estimated from the block model (Tab. S5).

Graphical abstract

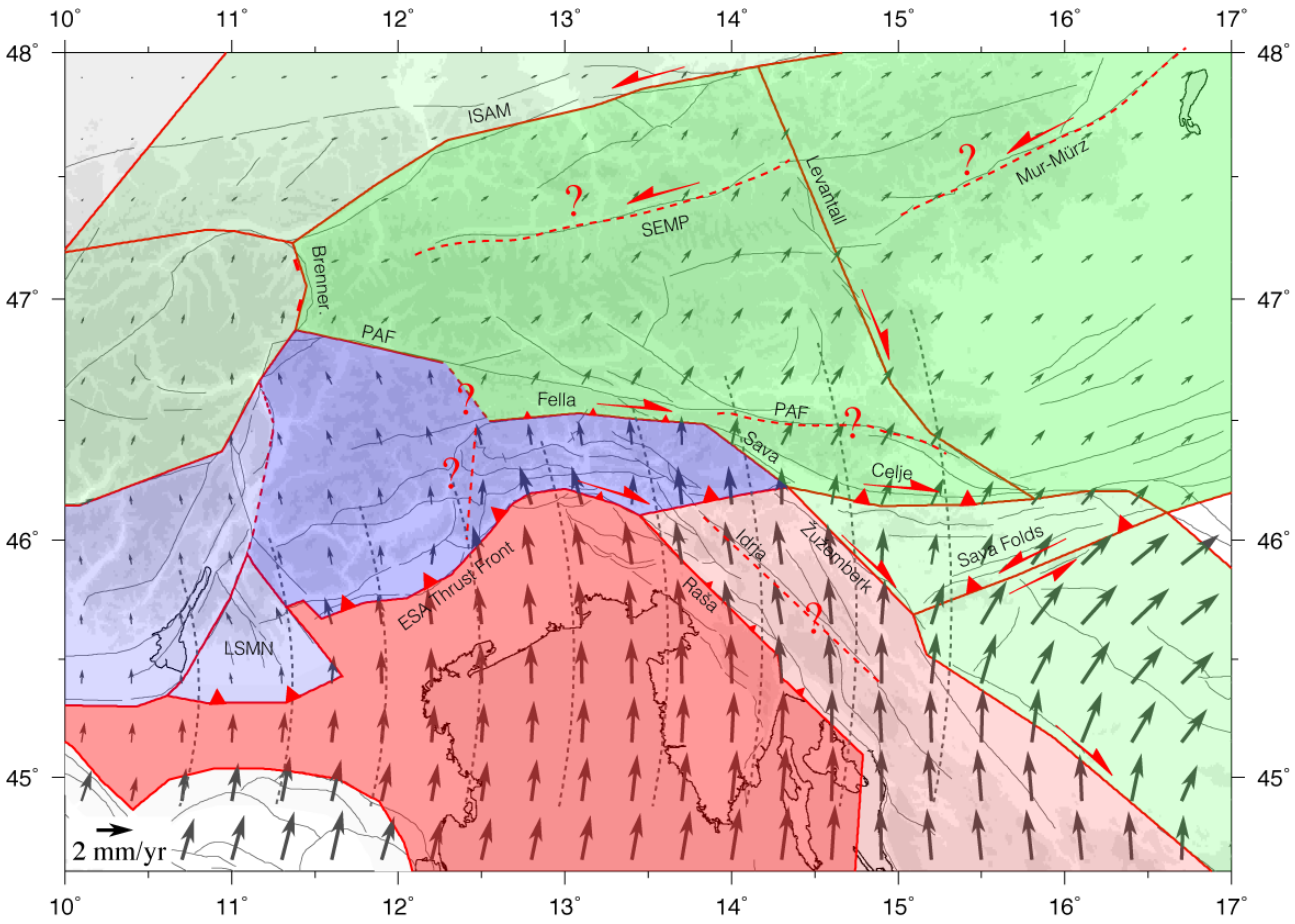

HIghlights

1) GPS and seismological data show consistent kinematics in the eastern Alps
2) Kinematics and tectonics result from the interplay of several tectonic blocks
3) GPS show new evidence for active deformation across faults
4) Limited interseismic coupling found for the Montello-Cansiglio thrust faults
5) New insights into seismic potential from seismic and geodetic moment rates